NTNU
Norwegian University of
Science and Technology

Planetary Wave Oscillations observed in Ozone and Temperature Data from Antarctica during 2009

Christine Birgitte Osnes

Master of Science in Physics and Mathematics
Submission date: June 2011
Supervisor: Patrick Joseph Espy, IFY

Norwegian University of Science and Technology
Department of Physics

Problem Description

Planetary waves have frequently been traced in the atmospheric regions up to the lower stratosphere and above the upper mesosphere, but measurements from the region between these two are generally sparse. Most of the middle and upper stratosphere, as well as the mesosphere belongs to an altitude range that is too high for the effective use of stratospheric measurement techniques and too low for most satellite measurements.

There are methods for measuring this part of the atmosphere, like LIDARs and falling spheres, but these are generally ill-suited for tracing atmospheric waves.

Millimeter wave spectrometry is another technique that can be used for measuring the middle atmosphere. Unlike falling spheres, this is a passive measuring-method able to continuously take measurements above a specific location. And unlike LIDARs, it does not make measurements relative to a given height, making it possible to trace the propagation of atmospheric waves in the data.

In this thesis, ozone data from the millimeter wave spectrometer ARON will be analyzed in order to search for planetary waves in the data. The same will be done to temperature data measured from the OH Meinel nightglow by a Michelson interferometer, a technique known to be able to observe the progress of planetary waves.

The results from the two datasets will be compared to previous observations of planetary waves, and to each other to see if the results from the millimeter wave spectrometer ozone data are similar to those of the temperature data and previous results. If this is the case, it will indicate that millimeter wave spectrometry is a viable technique for tracing planetary waves in the middle atmosphere.

Acknowledgments

Big thanks to my supervisor Patrick Espy for all the help, good ideas, enlightening explanations and amusing stories. Thanks also to Inger Skjærholt, for helping me in the fight against grammatical errors and bad spelling, and to my familiy for their support. Lastly, loads of thanks to Joakim for always being supportive and cheering me on, and for generally making my days better.

Abstract

In this thesis measurements of ozone and temperatures have been used to find planetary waves in the atmosphere above Antarctica during 2009.

The temperature data was obtained from ground based measurements of the brightness of the OH Meinel (3,1) band, measured at Rothera (68°S, 68°W). The ozone data was in the form of vertical ozone mixing ratio profiles up to 106km, retrieved from measurements of the 249.6GHz ozone line using the ground based millimeter-wave spectrometer ARON at Troll station (72°S, 2°E).

The ozone data covered the period from December 2008 to November 2009, with a time resolution of 1 hour and an altitude resolution of 8km. Temperature data covered the period from 2002 to November 2009, though only data from 2009 has been used. Temperatures were measured during the night at an altitude of 87km.

Planetary waves have previously been found in the ozone data obtained by millimeter wave spectrometry (Kleinknecht 2010). By comparing the observations of waves in ozone to observations in temperature data, the results from this method of measuring can be further tested to see if its results are in accordance with an already proven method of tracing planetary waves.

Seasonal variations were filtered out and the Lomb normalized periodogram was used to perform a spectral analysis of the data. Wave activity was found in the 4, 5, 8-9, 10-11, 11-13, 14-15, 17-20, 21-24 and 26-45 day bands, some of them possibly corresponding to known atmospheric normal modes, and each band was isolated to see how the different wave motions varied with time and altitude. Characteristics typical of the planetary wave normal modes were observed.

The observed wave activity was also consistent between the ozone and temperature data, indicating that millimeter wave spectrometry is a viable technique for tracing planetary waves in ozone, yielding results consistent with those obtained from temperature data from the OH Meinel (3,1) band in the hydroxyl airglow.

Contents

1 Introduction

Like other fluids, the atmosphere can contain wave-like motions. There are several different types, from small sound waves to planet-scale Rossby waves. They are generally created by some disturbance, like convection or a flow of air being obstructed by mountains, or in the case of the Rossby waves: due to variations in the Coriolis effect with latitude.

The most interesting waves for this thesis are the large Rossby waves, or planetary waves. These can have wavelengths of thousands of kilometers and periods of several days, and are assumed to be important to many large-scale atmospheric phenomena. For example, the stratospheric warming in the Southern Hemisphere during 2002 has been set in connection with an increase in planetary wave activity ahead of the warming (Krüger et al. 2005).

Measurements of planetary waves have frequently been made both for the troposphere and lower stratosphere-region, as well as for the high-altitude upper mesosphere and lower thermosphere region. Measurements of the troposphere and lower stratosphere can be made using aircraft, radar or instruments carried by balloons transmitting information back to the surface using radio equipment. However, measurements made using balloons or *radiosondes* are only possible up to altitudes of approximately 30km (Houghton 2002). In the upper mesosphere and lower thermosphere, measurements can be made using rockets, or as radar measurements from satellites.

Measurements of the region between these two, containing most of the stratosphere and the mesosphere, are much more sparse as this altitude range is too high for the effective use of stratospheric measurement techniques and too low for most satellite measurements. Two methods that have been used for measuring this region are LIDARs and falling spheres, but these are not very well suited for observing planetary waves.

LIDARs make measurements relative to a specific height. If there are variations in temperature and density at this height due to passing planetary waves, similar variations at other heights will all be removed, and the wave will not be visible in the measurements.

Falling spheres are balloons released from high altitude rockets, taking measurements as they descend. These are able to make the measurements required to observe planetary waves in the middle atmosphere, but they are expensive. Due to the high cost of these falling spheres, acquiring enough measurements to get an acceptable time resolution would be extremely expensive.

Measurements of the middle and upper stratosphere as well as the mesosphere can however be made using ground based remote sensing of ozone, using a millimeter wave spectrometer. This is a passive measuring-method that can only take measurements above a fixed location, but it can measure the atmosphere continuously, and is relatively inexpensive to install and maintain.

In this thesis, planetary waves are found from variations in ozone mixing ratio measured by such an instrument placed at the Troll station in Antarctica. Temperature measurements from Rothera are also used, and the results found from the two methods are used

together and compared. Since temperature data from the hydroxyl airglow previously has been successfully used to trace atmospheric waves, the consistency between the two datasets and comparison with previous results will give an indication of whether or not waves can be traced in the measured ozone data.

1.1 Progress of the text

First, some theory on planetary waves, the hydroxyl molecule and how temperature measurements can be found from hydroxyl airglow, as well as some theory on ozone and its distribution will be given. Then follows a description of the data that has been used, before the main analysis is presented. The analysis includes preparing and averaging the data, removing seasonal variations, identifying and isolating interesting oscillations in the data.

The isolated oscillations, their frequencies and development with time, as well as the consistency between the datasets will be presented and discussed in Chapter 5. Some larger features and fit with previous results and theories will also be discussed in this chapter.

2 Theory

Theory that has been found useful in this thesis includes an introduction into the theory of atmospheric waves, particularly the planetary Rossby waves. Then, a short description of the hydroxyl molecule and the hydroxyl layer is given, to explain how the temperature data was acquired. After that follows some theory on ozone, its composition, creation and destruction, including how the ozone mixing ratio varies with time and temperature. Lastly, a rough description of the vertical distribution of ozone and how it can be measured using millimeter wave spectroscopy is given.

2.1 Planetary Waves

Planetary waves are usually divided into two main groups. "Oscillations of the first class", include high-frequency buoyancy or gravity waves, able to propagate zonally in both directions. "Oscillations of the second class" are rotational Rossby waves, migrating at lower frequencies and only westward in relation to the local flow (Salby 1984)

The Rossby waves or *planetary waves* is the class of oscillations most interesting for this thesis. Their horizontal scale is thousands of kilometers, the vertical scale several kilometers and they have periods of several days. These waves are only possible in a rotating medium, so some wave-theory for a rotating system will be presented in order to describe planetary waves and their characteristics.

2.1.1 Equations of motion for the atmosphere

When looking only at the middle atmosphere, it can usually be assumed to be a continuous, isotropic, classical Newtonian fluid affected by gravity, friction, pressure gradients and the rotation of the Earth. In this case, Newton's second law leads to the Navier-Stokes equation. Following (Andrews 2000, Chapter 4.5) the Navier-Stokes equation for fluid flow in an inertial frame is

$$\frac{D\mathbf{u}}{Dt} = -\frac{1}{\rho}\nabla p - g\mathbf{k} + \frac{\eta}{\rho}\nabla^2\mathbf{u} \tag{1}$$

for a flow $\mathbf{u}$, where ρ is the density of the fluid, $\mathbf{k}$ is the unit vertical vector $(0, 0, 1)$, g is the acceleration of gravity and η is the dynamic viscosity.

For large-scale dynamics of the atmosphere it is most convenient to have the coordinate system fixed with respect to the Earth. Since this system is rotating, the Navier-Stokes equation (1) must be modified.

Supposing the frame rotates with a velocity $\mathbf{\Omega}$ with respect to the inertial frame and both frames have the z-axis in the direction of $\mathbf{\Omega}$. The relationship between time derivatives of a time dependent vector $\mathbf{A}(t)$ in the inertial and rotating frame is:

$$\left(\frac{d\mathbf{A}}{dt}\right)_I = \left(\frac{d\mathbf{A}}{dt}\right)_R + \mathbf{\Omega} \times \mathbf{A} \tag{2}$$

and

$$\left(\frac{d^2\mathbf{A}}{dt^2}\right)_I = \left(\frac{d^2\mathbf{A}}{dt^2}\right)_R + 2\mathbf{\Omega} \times \left(\frac{d\mathbf{A}}{dt}\right)_R + \mathbf{\Omega} \times (\mathbf{\Omega} \times \mathbf{A}) \tag{3}$$

If $\mathbf{A}$ is the position vector, $\mathbf{A} = \mathbf{r}$, the relation between acceleration in the inertial frame and acceleration, velocity and position in the rotating frame will be

$$\mathbf{a}_I = \mathbf{a}_R + 2\mathbf{\Omega} \times \mathbf{u}_R + \mathbf{\Omega} \times (\mathbf{\Omega} \times \mathbf{r}) \tag{4}$$

The second term of this relation, $2\mathbf{\Omega} \times \mathbf{u}_R$, is the Coriolis acceleration. The last term, $\mathbf{\Omega} \times (\mathbf{\Omega} \times \mathbf{r})$, is the centripetal acceleration. To get the Navier-Stokes equation for a rotating frame, the acceleration $\mathbf{a} = \frac{D\mathbf{u}}{Dt}$ is replaced with $\mathbf{a}_1$ from equation (4). This gives

$$\frac{D\mathbf{u}}{Dt} = -\frac{1}{\rho}\nabla p - 2\mathbf{\Omega} \times \mathbf{u} - \mathbf{\Omega} \times (\mathbf{\Omega} \times \mathbf{r}) - g\mathbf{k} + \frac{\eta}{\rho}[\nabla^2\mathbf{u} + \frac{1}{3}\nabla(\nabla\mathbf{u})] \tag{5}$$

where $\mathbf{u}$ now is the velocity in the rotating frame, and

$$\frac{D}{Dt} = \frac{\partial}{\partial t} + u\frac{\partial}{\partial x} + v\frac{\partial}{\partial y} + w\frac{\partial}{\partial z}$$

.

When looking at the Earth's atmosphere, it is most logical to use spherical coordinates, (r, θ, λ) where θ is the latitude and λ is the longitude. An incremental increase in distance in the eastward direction can be written as $dx = rcos\theta d\lambda$, a similar incremental increase in the northward direction as $dy = rd\theta$ and an incremental upwards increase as $dz = dr$, where $r = a + z$, r is the distance from the center of the Earth, a is the Earth's radius and z is the altitude above the surface.

By ignoring the centripetal acceleration and writing on component form, equation (5) becomes

$$\frac{Du}{Dt} - (2\Omega + \frac{u}{r\cos\theta})(v\sin\theta - w\cos\theta) + \frac{1}{\rho}\frac{\partial p}{\partial x} = F^{(x)} \tag{6}$$

$$\frac{Dv}{Dt} + \frac{wv}{r} + (2\Omega + \frac{u}{r\cos\theta})u\sin\theta + \frac{1}{\rho}\frac{\partial p}{\partial y} = F^{(y)} \tag{7}$$

$$\frac{Dw}{Dt} - \frac{u^2 + v^2}{r} - 2\Omega u\cos\theta + \frac{1}{\rho}\frac{\partial p}{\partial z} + g = F^{(z)} \tag{8}$$

with $F^{(x)}$,$F^{(y)}$ and $F^{(z)}$ being the eastward, northward and upward components of the frictional force.

2.1.2 Approximations

These three equations can be simplified somewhat. Since the thickness of the atmosphere is much smaller than the radius of the earth, r can be replaced with the Earth's radius a. This is called the *shallow water approximation*. In addition, there are some simplifications to each of the three equations.

For the first equation, (6), the zonal wind u will generally be small enough that $\frac{|u|}{a\cos\theta} << 2\Omega$ except very close to the poles where the cosine goes to zero. In addition, vertical velocities are generally much smaller than horizontal velocities, making $|w\cos\theta| << |v\sin\theta|$, except close to the equator, where the sine goes to zero. Making these two simplifications and introducing the Coriolis parameter $f = 2\Omega\sin\theta$, the first of the three equations becomes

$$\frac{Du}{Dt} - fv + \frac{1}{\rho}\frac{\partial p}{\partial x} = F^{(x)} \tag{9}$$

For the second equation, (7), the term $\frac{|u|}{a\cos\theta}$ can still be said to be much less than 2Ω. In addition, the sizes of the velocities v and w are negligible compared to the radius of the earth, making $\frac{|wv|}{r} << 2\Omega|u\sin\theta|$, except near the equator. This makes the second equation simplify to

$$\frac{Dv}{Dt} + fu + \frac{1}{\rho}\frac{\partial p}{\partial y} = F^{(y)} \tag{10}$$

with f still being the Coriolis parameter.

For the third equation, (8), $\frac{(u^2+v^2)}{a}$ and $2\Omega u\cos\theta$ will both be much smaller than g for the reasonable values of u and v. In addition, the term for vertical friction $F^{(z)}$ is usually regarded as negligible. These simplifications then give

$$\frac{Dw}{Dt} + \frac{1}{\rho}\frac{\partial p}{\partial z} + g = 0 \tag{11}$$

for the third equation.

Since the waves of interest to this thesis are the planetary waves, which are very large-scale motions, the three equations can be simplified even further by looking at the scale of the different terms.

Starting with the first of the three simplified equations, (9): For motions of horizontal scale approximately 1000km = 10^6m, vertical scale of 10km= 10^4m, horizontal velocities on the scale of 10m/s, vertical velocities of approximately 10^2m/s and time scales of approximately one day, 10^5s

$$\frac{\partial u}{\partial t} \sim 10^4, \quad u\frac{\partial u}{\partial x} \sim 10^{-4}, \quad w\frac{\partial u}{\partial z} \sim 10^{-5}$$

and

$$fv = 2\Omega v \sin\theta \sim 10^{-3}$$

for θ in the mid-latitudes and with a negligible $F^{(x)}$. fv is the biggest term, and has to balance against $\frac{1}{\rho}\frac{\partial p}{\partial x}$,

$$fv = \frac{1}{\rho}\frac{\partial p}{\partial x}. \tag{12}$$

This simplification is called the geostrophic approximation. Similarly, the second of the three simplified equations (10) can be simplified further to

$$-fu = \frac{1}{\rho}\frac{\partial p}{\partial y}. \tag{13}$$

Together these two are the geostropic balance, where horizontal pressure gradients and Coriolis forces for horizontal winds balance each other. The third equation, (11) simplifies to the hydrostatic balance,

$$\frac{\partial p}{\partial z} = g\rho \tag{14}$$

The ratio between the inertial and Coriolis' forces is a dimensionless number R_0, called the Rossby number.

$$\frac{u\frac{\partial u}{\partial x}}{fv} \sim \frac{\frac{U^2}{L}}{fU} = \frac{U}{fL} \equiv R_0, \tag{15}$$

where U is the horizontal velocity, L is the horizontal scale of the phenomenon being looked at and f the Coriolis parameter, $f = 2\Omega\sin\theta$. For Rossby numbers much smaller than one, the Coriolis term is relatively small, while for Rossby numbers much larger than 1, the Coriolis term is large and the geostrophic approximation is usually valid.

2.1.3 The Boussinesq approximation and linearization

Equations (9),(10) and (11) are still quite complicated, and in order to simplify them further, the Boussinesq approximation is introduced (Andrews 2000, Chapter 5.2). This says that density differences in the atmosphere might be neglected, except for deep layers or where the density differences appear in terms multiplied by g. For the first two of the equations mentioned, the Boussinesq approximation simply means that the density ρ is replaced by a constant value ρ_0:

$$\frac{Du}{Dt} - fv + \frac{1}{\rho_0}\frac{\partial p}{\partial x} = F^{(x)} \tag{16}$$

$$\frac{Dv}{Dt} + fu + \frac{1}{\rho_0}\frac{\partial p}{\partial y} = F^{(y)}. \tag{17}$$

The third equation, (11) can be approximated by hydrostatic balance, as done before:

$$\frac{\partial p}{\partial z} = -g\rho. \tag{18}$$

For an incompressible flow, the density is constant while following a moving fluid parcel. However, vertical density stratification must still be allowed, and it is therefore convenient to separate the density into two parts, one for the background, which only depends on the height z, plus a deviation. The same separation can be done for the pressure, giving that $p(x, y, z, t) = \overline{p}(z) + p'(x, y, z, t)$, where $\overline{p}(z)$ is the background and $p'(x, y, z, t)$ is the deviation. If it is assumed that the background pressure satisfies hydrostatic balance, then it is implied from equation (18) that the same is true for the deviation:

$$\frac{\partial p'}{\partial z} = -g\rho'. \tag{19}$$

If the atmosphere is thus seen as incompressible, the mass-continuity equation

$$\frac{D\rho}{Dt} + \rho\nabla \cdot \mathbf{u} = 0 \tag{20}$$

can be decoupled into

$$\frac{D\rho}{Dt} = 0, \quad \nabla \cdot \mathbf{u} = 0. \tag{21}$$

When the density is seen as $\rho(x, y, z, t) = \overline{\rho}(z) + \rho'(x, y, z, t)$ and substituted into the first part of (21), the result is

$$\frac{D\rho'}{Dt} + w\frac{d\overline{\rho}}{dz} = 0 \tag{22}$$

where a buoyancy frequency $N_B(z)$ is introduced for the stratified, incompressible fluid:

$$N_B^2 = -\frac{g}{\rho_0}\frac{d\overline{\rho}}{dz} \tag{23}$$

giving that

$$g\frac{D\rho'}{Dt} - \rho_0 N_B^2 w = 0 \tag{24}$$

or

$$\frac{D}{Dt}\left(-\frac{g\rho'}{\rho_0}\right) + N_B^2 w = 0. \tag{25}$$

Equations (16), (17), (19) and (25), together with

$$\frac{\partial u}{\partial x} + \frac{\partial v}{\partial y} + \frac{\partial w}{\partial z} = 0 \tag{26}$$

are called the Boussinesq equations. These are nonlinear and quite tricky to solve without the use of computers. However, they can be linearized, by assuming that all velocities and deviations are small, so that quadratic terms of these and their derivatives can be neglected. By ignoring all these terms and assuming friction to be negligible the horizontal momentum equations and the hydrostatic equation can be found:

$$\frac{\partial u}{\partial t} - fv + \frac{1}{\rho_0}\frac{\partial p'}{\partial x} = 0 \tag{27}$$

$$\frac{\partial v}{\partial t} + fu + \frac{1}{\rho_0}\frac{\partial p'}{\partial y} = 0 \tag{28}$$

$$\frac{\partial u}{\partial x} + \frac{\partial v}{\partial y} + \frac{\partial w}{\partial z} = 0 \tag{29}$$

$$-\frac{g}{\rho_0}\frac{\partial \rho'}{\partial t} + N_B^2 w = 0 \tag{30}$$

$$\frac{\partial p'}{\partial z} + g\rho' = 0. \tag{31}$$

2.1.4 Linear wave theory

From here on, (Forbes 1995) will be followed. In an atmosphere assumed to be horizontally stratified, zonal mean winds are zero and the linearized equations describing atmospheric motions can be decoupled. Further simplification can be done by assuming the background atmosphere to be isothermal. This leads to the linearized equations for perturbations on a spherical isothermal atmosphere:

$$\frac{\partial u}{\partial t} - 2\Omega \sin\theta v + \frac{1}{a\cos\theta}\frac{\partial \Phi}{\partial \lambda} = 0 \tag{32}$$

$$\frac{\partial v}{\partial t} + 2\Omega \sin\theta u + \frac{1}{a}\frac{\partial \Phi}{\partial \theta} = 0 \tag{33}$$

$$\frac{\partial}{\partial t}\Phi_z + N^2 w = \frac{\kappa J}{H} \tag{34}$$

$$\frac{1}{a\cos\theta}\left[\frac{\partial u}{\partial \lambda} + \frac{\partial}{\partial \theta}(v\cos\theta)\right] + \frac{1}{\rho_0}\frac{\partial}{\partial z}(\rho_0 w) = 0 \tag{35}$$

where the variables are

u	eastward velocity
v	northward velocity
w	upward velocity
Φ	perturbation geopotential
N^2	buoyancy frequency squared, $\kappa g/H$
Ω	angular velocity of the Earth
ρ_0	basic state density $\propto e^{-z/H}$
z	altitude
λ	longitude
θ	latitude
κ	$R/c_p \approx 2/7$
J	heating per unit mass
a	radius of the Earth
g	acceleration due to gravity
H	constant scale height
t	time

It can be assumed that any perturbations consist of longitudinally propagating waves with zonal wavenumber s and frequency σ:

$$\{u, v, w, \Phi\} = \{\hat{u}, \hat{v}, \hat{w}, \hat{\Phi}\}\exp[i(s\lambda - \sigma t)] \tag{36}$$

The zonal wavenumber describes the number of maxima the sinusoidal oscillation has in the longitudinal direction, with possible values zero or positive integers. Positive values of the frequency σ correspond to eastward propagating waves, while negative values correspond to westward propagation.

Inserting equation (36) into equations (32)-(35) removes all differentials with respect to t and λ, and gives a single second-order partial differential equation for Φ in altitude and latitude. Separable solutions can then be found in the form

$$\hat{\Phi} = \sum_n \Theta_n(\theta) G_n(z) \tag{37}$$

$$\hat{J} = \sum_n \dot{\Theta}_n(\theta) J_n(z) \tag{38}$$

$$\hat{u} = \frac{\sigma}{4\Omega^2 a} \sum_n U_n(\theta) G_n(z) \tag{39}$$

$$\hat{u} = \frac{-i\sigma}{4\Omega^2 a} \sum_n V_n(\theta) G_n(z) \tag{40}$$

where $\{\Theta_n\}$ is a complete orthogonal set and the zonal and meriodinal velocity expansion functions U_n and V_n are derivations of Θ_n:

$$U_n = \frac{1}{(f^2 - \sin^2\theta)} \left[\frac{s}{\cos\theta} + \frac{\sin\theta}{f} \frac{d}{d\theta} \right] \Theta_n \tag{41}$$

$$V_n = \frac{1}{(f^2 - \sin^2\theta)} \left[\frac{s\tan\theta}{f} + \frac{d}{d\theta} \right] \Theta_n. \tag{42}$$

The expression

$$i\sigma H \left[\frac{1}{\rho_0} \frac{\partial}{\partial z} \rho_0 \frac{\partial}{\partial z} G_n \right] + \frac{1}{\rho_0} \frac{\partial}{\partial z} (\rho_0 \kappa J_n) = -\frac{i\sigma\kappa}{h_n} G_n \tag{43}$$

is a consequence of separation, with h_n as a separation constant. Using $x = z/H$, and $H = 7.5$km, corresponding to a T_0 of 256K, in an isothermal atmosphere, it is possible to define $G'_n = G_n \rho_0^{1/2} N^{-1}$ with $N^2 = \kappa g/H$. This gives the vertical structure equation for an isothermal atmosphere:

$$\frac{d^2 G'_n}{dx^2} + \left[\frac{\kappa H}{h_n} - \frac{1}{4} \right] G'_n = -\frac{\rho_0^{-1/2}}{i\sigma N} \frac{d}{dx} (\rho_0 J_n). \tag{44}$$

The latitude-dependent part of the solution is embodied in Laplace's tidal equation

$$\frac{d}{d\mu} \left[\frac{(1-\mu^2)}{(f^2 - \mu^2)} \frac{d\Theta_n}{d\mu} \right] - \frac{1}{f^2 - \mu^2} \left[-\frac{s}{f} \frac{(f^2 + \mu^2)}{(f^2 - \mu^2)} + \frac{s^2}{1-\mu^2} \right] \Theta_n + \epsilon \Theta_n = 0 \tag{45}$$

where $\mu = \sin\theta$ and $\epsilon = (2\Omega a)^2/g h_n$. Through this, the equations governing atmospheric perturbations are formulated as an eigenfunction-eigenvalue problem. Either ϵ_n or h_n can be referred to as the eigenvalues of the system, and equations (44) and (45) are linked through the set of values h_n, usually referred to as the *equivalent depth.*

Laplace's equation can be reformulated as

$$f_{s,\nu}(\Theta_n^{s,\nu}) = \epsilon_n^{s,\nu} \Theta_n^{s,\nu} \tag{46}$$

with s as the zonal wavenumber and $\nu = \sigma/\Omega$ the normalized frequency, making the eigenfunction-eigenvalue problem more obvious. Again, positive values of the frequency

correspond to eastward propagation and negative values to westward propagation. The eigenfunctions Θ_n are called Hough functions and represent the horizontal structure of the wave.

Each eigenfunction/eigenvalue pair constitutes a *wave mode*. These are usually identified by their zonal wave number s, meridional wave number n and usually some information about the normalized frequency or period as well. It is common to refer to a given wave as the (s, n) wave, or the $(s, |n| - s)$ wave, including some information about the wave period. Alternatively, a given wave can be referred to as for example the *first symmetric* or *second antisymmetric*, where symmetric or antisymmetric tells whether $n - s$ is an odd or even number, with *first* or *second* referring to which symmetric or antisymmetric mode it is. For Rossby waves, modes with odd $|n| - s$ are symmetric around the equator, while even $|n| - s$ are antisymmetric.

2.1.5 Forced and free solutions of the vertical structure equation

Equation (44) can be rewritten as

$$\frac{d^2 G'_n}{dx^2} + \alpha^2 G'_n = F(x) \tag{47}$$

where

$$\alpha = \pm\sqrt{\kappa H/h_n - 1/4}. \tag{48}$$

This has solutions on the form $G'_n \sim Ae^{i\alpha x} + Be^{-i\alpha x}$. There are two types of solutions, *forced solutions* if $F(x) \neq 0$ and *free solutions* if $F(x) = 0$.

Forced solutions The forced solutions again separated into two different types. If $h_n < 0$ or $h_n > 4\kappa H$, α^2 will be negative and $G'_n \sim e^{-|\alpha|x}$ above the source region. These waves are usually referred to as *trapped* or *evanescent*, and are usually confined to the region where they were excited.

If $0 < h_n < 4\kappa H$, then α^2 will be positive, and $G'_n \sim e^{i\alpha x}$. This is a propagating solution, where the waves propagate away from their source region. α is chosen to be positive for waves with an eastward propagation, and negative for westward propagation waves.

Free solutions When $F(x) = 0$, any resulting waves have a zero total forcing, and occur due to random forcings. With $F(x) = 0$ the only nontrivial solution satisfying boundedness and a zero velocity at ground level is

$$G'_n \sim e^{(\kappa - \frac{1}{2})x} \tag{49}$$

with

$$h_n = \frac{H}{1-\kappa}. \tag{50}$$

This free solution corresponds to a resonant response of the atmosphere. It also implies energy decay away from the surface and an exponential increase of the horizontal velocity and other wave fields with altitude. For negative values of α^2 there is no vertical flux of energy out of the atmosphere, and no phase change with height.

The free modes are also known as *normal modes*. As mentioned, these are resonant modes of an ideal atmosphere and have no downward phase progression and no change of amplitude with height. In contrast, the amplitude of propagating waves increases with altitude due to the exponential decrease in air density combined with energy conservation.

Classification of wave modes As mentioned, Laplace's equation can be written as $f_{s,\nu}(\Theta_n^{s,\nu}) = \epsilon_n^{s,\nu}\Theta_n^{s,\nu}$ to make the eigenfunction-eigenvalue problem more obvious. For each choice of zonal wavenumber s and normalized frequency ν there are sets of ϵ_n and Θ_n that satisfy both Laplace's equation and the condition of boundedness at the poles.

The eigenvalues and frequencies are generally related parametrically for a given zonal wavenumber. An example for the zonal wavenumber $s = 1$ can be seen in Figure 1.

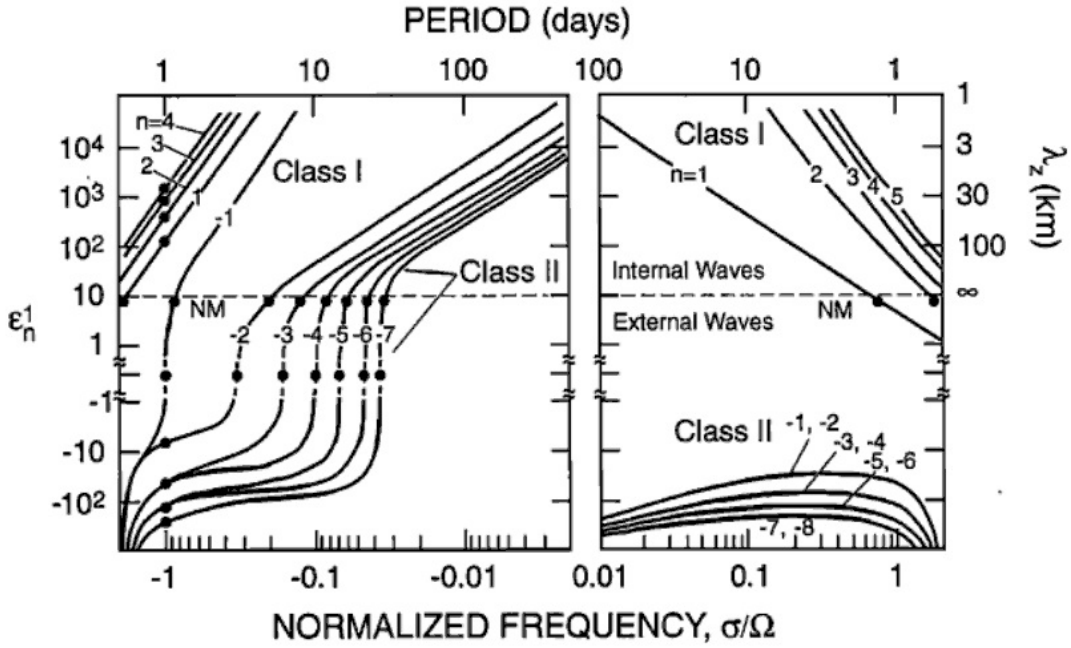

Figure 1: Eigenvalues of ϵ_n^s for wave modes of zonal wavenumber s = 1 vs. normalized frequency $\nu = \sigma/\Omega$. Positive (negative) frequencies propagate to the east (west). The dots labeled NM refer to the normal modes. Class I are gravity waves and class II are planetary waves. From (Forbes 1995)

Two families of curves can be seen, both for eastward ($\sigma > 0$) and westward ($\sigma < 0$) propagating waves. Class I are *gravity modes* and class II are *planetary wave modes*. The gravity waves have positive meridional wave numbers n, while planetary waves have negative meridional wave numbers. The planetary waves also have positive eigenvalues for westward propagation and negative for all other cases. The (1,-1) mode behaves like a gravity wave for large and positive eigenvalues and like a planetary wave for large and negative eigenvalues. This mode is often called the *mixed*, or *Rossby-Gravity* mode.

2.1.6 Rossby waves

As previously mentioned, planetary waves or Rossby waves stretch horizontally over thousands of kilometers and have periods of several days. They are formed by a combination of temperature gradients and the rotation and curvature of the Earth.

In section 2.1.4 the usual nomenclature for these waves was mentioned. They are said to be symmetric around the equator if the difference between the meridional and zonal wavenumber ($|n| - s$) is odd, and antisymmetric if it is even. In addition, the number $|n| - s$ describes which symmetric or antisymmetric mode it is. $|n| - s = 1$ would be the first symmetric, with $|n| - s = 3$ being the second symmetric, etc. Some common westward traveling waves can be found in Table 2.1.6.

Quasi-period	(s,n)	$(s, \lvert n\rvert - s)$	Additional description
2-day	(3,-3)	(3,0)	Mixed Rossby-Gravity, antisymmetric
4-day	(2,-3)	(2,1)	Rotational Rossby, first symmetric
5-day	(1,-2)	(1,1)	Rotational Rossby, first symmetric
10-day	(1,-3)	(1,2)	Rotational Rossby, first antisymmetric
16-day	(1,-4)	(1,3)	Rotational Rossby, second symmetric

Table 1: Some common westward traveling waves in the middle and upper atmosphere. From (Forbes 1995)

The effect of winds The waves will be influenced by winds. If it is assumed that there is a mean eastward wind $\overline{U}\sin\theta$, then the frequency σ should be replaced by the Doppler-shifted frequency σ_D. The same would be the case for the normalized frequency ν, becoming ν_D.

For an observer on the ground, the apparent wave frequency would be

$$\sigma_{obs} = \sigma_D + k\overline{U} \tag{51}$$

where k is the zonal wavenumber divided by the radius of the Earth, $k = s/a$. The corresponding observed period is

$$T_{obs} = \frac{2\pi}{|\sigma_D + k\overline{U}|}. \tag{52}$$

Because of this it is expected that the free Rossby modes will be Doppler-shifted to longer periods by an eastward wind. For example, the observed periods for the 5, 10 and 16-day waves are closer to 5.6, 10.2 and 17.1 days for $\epsilon = 8.4$ (Forbes 1995). This is the reason for them often being named the "quasi 5-day wave" etc.

The effect of mean winds increases with decreasing phase speeds of the waves. For Rossby waves, as the wave periods increase, the phase speeds decrease, making the waves more susceptible to effects of mean winds.

If T is the wave period in days, then westward propagating planetary waves will have phase speeds

$$c_p = -\frac{\Omega a \sin\theta}{sT} \tag{53}$$

while stationary planetary waves have $c_p = 0$.

Vertical propagation of stationary planetary waves is only possible in eastward winds, as long as the wind speed is below an upper limit. This is also the case for propagating planetary waves, but in this case the wind no longer has to be strictly eastward, only eastward relative to the wave, $\overline{U} - c_p > 0$.

As mentioned, strong eastward winds are able to stop traveling planetary waves. So stationary planetary waves can only travel in a small range of mean flows,

$$0 < \overline{U} < U_c \tag{54}$$

where the critical velocity U_c is given by the Charney-Drazin criterion:

$$U_c = \frac{\beta}{[(s^2 + n^2) + \frac{f_0^2}{4H^2N^2}]} \tag{55}$$

with H being the scale height, and N the buoyancy or Brunt-Vaisälä frequency (Salby 1996).

The phase speed of planetary waves is always westward relative to the background flow, but the group velocity c_g can be either westward or eastward.For long zonal wavelengths, the group propagation relative to the medium will be quickly westward, while for short zonal wavelengths the group propagation will be slowly eastward (Lynch and Cassano 2006).

If a planetary wave enters an area where the mean wind is westward with respect to the zonal phase velocity c_p, the wave energy will be absorbed and the frequency and group velocity of the wave vanishes.

2.2 Hydroxyl

At an altitude of about 87km there is a 6-8km thick layer of excited hydroxyl (OH*). This layer emits radiation in the near-infrared, which can be observed, and since the low-level rotational levels of excited hydroxyl can be assumed to be in thermal equilibrium

with its surroundings (Pendleton et al. 1993), the radiation can be used to find the temperature at the height of the hydroxyl layer. The data used in this thesis was found from measurements of the hydroxyl Meinel (3,1) band, or the frequency produced by rotational-vibrational transitions from vibrational level $v = 3$ to vibrational level $v = 1$.

Excited hydroxyl is mainly produced by the reaction

$$H + O_3 \rightarrow OH^* + O2 \tag{56}$$

with the production rate

$$P(OH^*) = k_{H+O_3}[H][O_3] \tag{57}$$

and with loss being through radiation

$$L(OH) = A[OH]. \tag{58}$$

During the night, the production of excited hydroxyl is the major reaction responsible for loss of ozone, so the concentration of hydroxyl will be proportional to the concentration of ozone. Ozone is mainly created through the recombination of atomic and molecular oxygen,

$$P(O_3) = k_{O+O_2+M}[O][O_2][M] \tag{59}$$

where M is an arbitrary air molecule. In a steady state, the production will equal the loss. For hydroxyl this means that

$$[OH]A = k_{H+O_3}[H][O_3] \tag{60}$$

and for ozone

$$k_{O+O_2+M}[O][O_2][M] = k_{H+O_3}[H][O_3] \tag{61}$$

Combining these two gives

$$[OH]A = k_{O+O_2+M}[O][O_2][M], \tag{62}$$

or that the radiation from excited hydroxyl is proportional to the concentration of atomic and molecular oxygen. The density of molecular oxygen decreases with height, while atomic oxygen is only found above a certain height, with a peak around 95-100km (Espy 2010). Since the concentrations of ozone and hydroxyl depend both on molecular and atomic oxygen, the hydroxyl layer will be situated somewhat lower than the maximum density of atomic oxygen.

2.2.1 The hydroxyl molecule

An atom or molecule can only exist in energy states with discrete values. For a molecule consisting of a single atom, the energy states are given by the quantum number, or the electronic energy. If a such an atom moves from one energy state to another state with lower energy, the energy-difference can be radiated away in the form of a photon, with energy

$$h\nu = E_2 - E_1 \tag{63}$$

where h is Planck's constant, ν is the frequency of the emitted photon, E_2 is the initial energy state and E_1 is the final energy state of the atom. The wavelength of the emitted photon is simply $\lambda = hc/(E_2 - E_1)$.

For diatomic molecules like hydroxyl it is somewhat more complicated. These molecules have both electronic, rotational and vibrational energy states. The energy of the molecule can then be seen as a sum of these three

$$E = E_e + E_v + E_r \tag{64}$$

The easiest way of looking at rotation of a diatomic molecule is as a rigid rotator,

$$E = \frac{1}{2} I\omega^2 \tag{65}$$

where ω is the angular velocity of the rotation and I is the moment of inertia. For the dumbbell model this is

$$I = m_1 r_1^2 + m_2 r_2^2 \tag{66}$$

$$r_1 = \frac{m_2}{m_1 + m_2} r, \quad r_1 = \frac{m_1}{m_1 + m_2} r \tag{67}$$

which gives the discrete energy-values

$$E = \frac{h^2 J(J+1)}{8\pi^2 I} \tag{68}$$

where J is the rotational quantum number. The discrete energy levels from rotation have energies that increase quadratically with the rotational quantum number (Hertzberg 1950).

In addition to the rotational and electronic energies, the molecule will also have vibrational energies. The simplest way to model vibrations in a diatomic molecule is as a harmonic oscillator. A classical harmonic oscillator can be described by

$$F = -kx = m\frac{d^2x}{dt^2} \tag{69}$$

In a harmonic oscillator the potential energy is proportional to the square of the distance from its equilibrium position; the potential energy curve is a parabola. For the diatomic molecule, the restoring force exerted by the two atoms on each other will be approximately proportional to the change in distance between the two nuclei, and for each atom we will get

$$m\frac{d^2r}{dt^2} = -k(r - r_e), \tag{70}$$

or for the entire oscillator

$$\mu\frac{d^2(r - r_e)}{dt^2} = -k(r - r_e) \tag{71}$$

where μ is the reduced mass. From here it is given that the classical vibrational frequency of the molecule will be

$$\nu_{osc} = \frac{1}{2\pi}\sqrt{\frac{k}{\mu}}. \tag{72}$$

The only possible energy-values are those energies where

$$E(v) = \frac{h}{2\pi}\sqrt{\frac{k}{\mu}(v + \frac{1}{2})} = h\nu_{osc}(v + \frac{1}{2}), \tag{73}$$

the vibrational quantum number v only takes integral values. The energy values can be transformed to term values G by dividing by hc,

$$G(v) = \frac{E(v)}{hc} = \frac{\nu_{osc}}{c}(v + \frac{1}{2}) \tag{74}$$

and in band spectroscopy ν_{osc}/c is generally designated ω, giving

$$G(v) = \omega(v + \frac{1}{2}) \tag{75}$$

where ω is the vibrational frequency, in [cm^{-1}] (Hertzberg 1950). Some corrections have to be made to this, as the molecule is not a perfect harmonic oscillator. Seeing the molecule as an anharmonic oscillator makes the term values

$$G(v) = \omega_e(v + \frac{1}{2}) - \omega_e x_e(v + \frac{1}{2})^2 + \omega_e y_e(v + \frac{1}{2})^3 + ... \tag{76}$$

This means that the energy levels of an anharmonic oscillator are not equally distanced, but get closer for higher vibrational quantum numbers.

For each vibrational level, there are several rotational levels. If a molecule makes a transition from one purely vibrational level to another, this gives a pure vibration spectrum. If the molecule can also change its rotational level at the same time, this is a rotational-vibrational transition and gives the rotation-vibration spectrum (Lund 2010). The OH Meinel (3,1) band is the rotation-band given by a rotational-vibrational transition from vibrational level 3 to vibrational level 1, named after Meinel, who was the first to observe OH-emissions in the nightglow (Sivjee 1992).

When hydroxyl is created it is mostly in high vibrational states. The reaction that creates OH^* releases $3,34$eV of energy, which makes it possible to reach vibrational levels up to $v = 9$. The production of OH^* creates excited hydroxyl in the states v = 6,7,8 and 9 (Sivjee 1992). These excited states can radiate and fall to lower vibrational states through vibrational-rotational transitions, or they can collide with other molecules and transfer vibrational energy to the other molecule, and thereby fall to lower states. This is how excited hydroxyl in vibrational state 3 is created. When these radiate and fall to vibrational state 1, the OH Meinel (3,1) band is created.

The excited hydroxyl molecules have a relatively long radiative lifetime and will on average collide at least ten times before emitting a photon (Sivjee 1992). It can therefore be said that the excited hydroxyl will be in thermal equilibrium with the surroundings, and any information about temperature given by the radiation will not only describe the OH^*-molecules but also their surroundings.

The intensity of each rotational line from the hydroxyl night glow can be expressed as

$$I(v', v'', J', J) = A(v', v'', J', J)C(v', J')(2J' + 1)e^{-E(v',J')kT} \tag{77}$$

where $A(v', v'', J', J)$ are Einstein coefficients for a spontaneous emission from one rotational and vibrational state to another, and $C(v', J')$ is the population of the v' state, (Sivjee 1992). From this, and knowledge of the population of the v'-state it is possible to find an estimate for the temperature.

2.3 Ozone

Though it is only a minor constituent in the atmosphere, ozone plays an important role in protecting life on Earth by filtering out certain types of UV radiation that would otherwise be harmful. In addition, together with long wavelength cooling to space from CO_2, short-wave heating due to ozone absorption controls the radiative energy budget, and thus the thermal structure of the middle atmosphere. This makes ozone one of the most important constituents of the middle atmosphere.

In this thesis, measurements of the ozone mixing ratio will be used to trace the propagation of planetary waves. The mixing ratio of ozone will change due to passing planetary waves and other dynamical and chemical processes throughout the year.

While the amount of column ozone is quite stable at low latitudes, there are large seasonal variations at higher latitudes, see Figure 2. The most well-known of these is probably the reduction of ozone observed in the Antarctic stratosphere during the southern hemisphere spring, the Antarctic ozone hole. In order to be able to observe planetary waves in the ozone data, such seasonal variations must be removed.

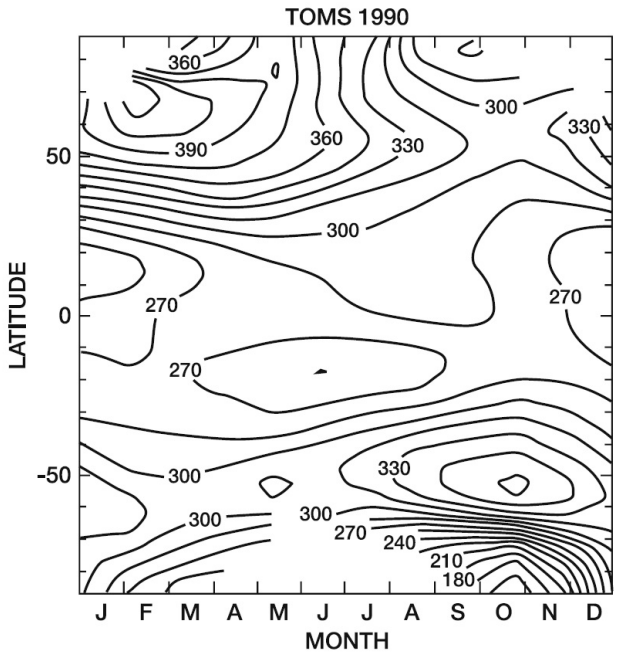

Figure 2: Variation of total ozone (DU) with latitude and season in the year 1990, as measured by the TOMS instrument. From (Brasseur and Solomon 2005)

The chemistry in this section is mainly based on (Andrews 2000), (Brasseur and Solomon 2005) and (Salby 1996).

2.3.1 The ozone molecule and ozone chemistry

An ozone molecule consists of three oxygen atoms bonded together, and is much less stable than the more common molecular oxygen, O_2. The first description of the chemical reactions of ozone was made by Chapman in 1930, and consists of a set of oxygen-only reactions. Later, catalytic processes were added. In the following equations, k_i are chemical rate coefficients and j_i are photodissociation rate coefficients of the various processes.

Chapman chemistry The starting point of Chapman's oxygen-only processes is molecular oxygen being photodissociated by UV radiation with wavelengths shorter than 242.4nm (Brasseur and Solomon 2005).

$$O_2 + h\nu \rightarrow 2O \quad (j_2) \tag{78}$$

followed by the atomic oxygen recombining with O_2 to create ozone in the fast reaction

$$O_2 + O + M \rightarrow O_3 + M \quad (k_2). \tag{79}$$

M here represents an arbitrary molecule that carries off the excess energy and momentum from the combination of atomic and molecular oxygen.

Ozone can be destroyed through photodissociation by UV radiation, recombination with atomic oxygen or catalytic processes. Photolytic destruction,

$$O_3 + h\nu \rightarrow O_2 + O \quad (j_3) \tag{80}$$

requires UV-radiation with wavelengths of 1140nm or less, and is another fast reaction. If there are enough other molecules in the vicinity, the atomic oxygen created by equation (80) will quickly recombine with molecular oxygen in equation (79), in a cycle that absorbs solar energy without losing any of the oxygen molecules. This is how ozone is able to shield from harmful UV radiation.

Ozone being destroyed through recombination with atomic oxygen is through the slow reaction

$$O_3 + O \rightarrow 2O_2 \quad (k_3) \tag{81}$$

and is strongly dependent on temperature.

Equations (78) and (79) have the net effect of producing ozone from molecular oxygen,

$$3O_2 \rightarrow 2O_3 \tag{82}$$

while equations (80) and (81) have the reverse net effect of destroying ozone and giving molecular oxygen

$$2O_3 \rightarrow 3O_2 \tag{83}$$

Diurnal variations In the upper mesosphere, atomic oxygen is more abundant than ozone. At these heights, the ozone is short-lived due to high photolysis rates that further increase with altitude. In contrast, the lifetime of atomic oxygen increases with altitude due to slower recombination.

Below 85km the lifetime of atomic oxygen is rather short, and when the sun sets and the photolytic destruction of ozone stops, the atomic oxygen quickly disappears as it recombines into ozone. This leads to the concentration of ozone increasing after sunset, and then staying high for the rest of the night. When the sun rises, the photolytic destruction of ozone starts up again, and the excess ozone disappears until the ozone and atomic oxygen once again are in photochemical equilibrium.

In the middle and lower stratosphere, the concentrations of atomic oxygen are very small, and the photolysis rates of ozone are much less than at higher altitudes, leading to ozone lifetime of a day or more. Due to this, the diurnal variations in the stratosphere are relatively small compared to those at higher altitudes (Brasseur and Solomon 2005).

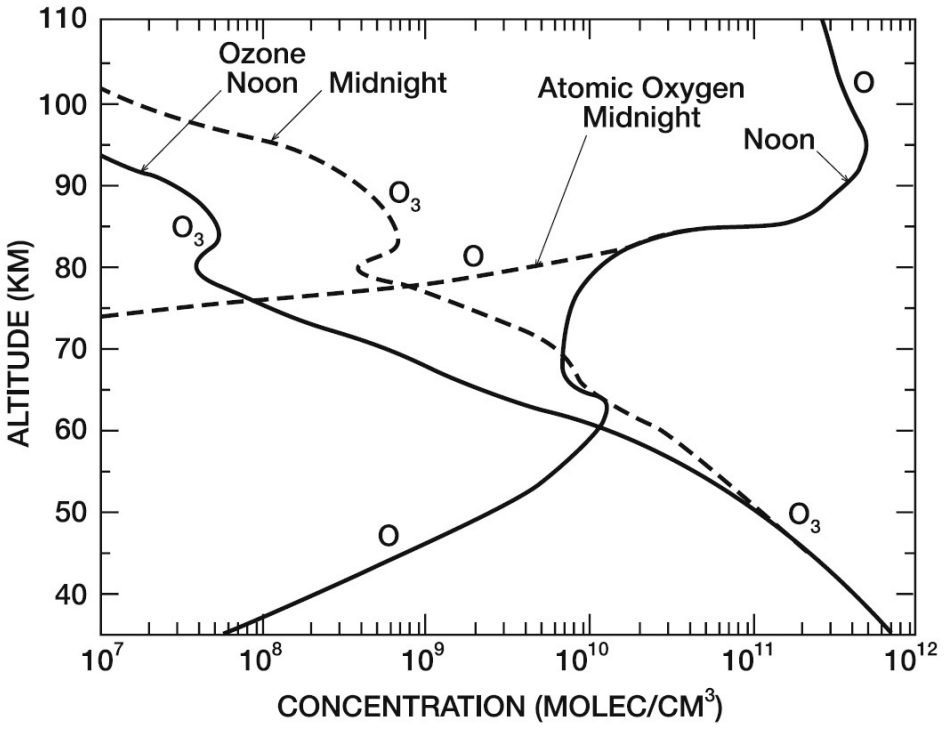

Figure 3: Calculated vertical distributions of ozone and atomic oxygen at noon and midnight. From (Brasseur and Solomon 2005).

Catalytic cycles In addition to photo dissociation and recombination with atomic oxygen, ozone might also be destroyed by photochemically active, free radicals. These destroy ozone in catalytic circles that leave the free radicals unchanged. A typical catalytic cycle would be

$$X + O_3 \rightarrow XO + O_2 \quad (k_4) \tag{84}$$

$$XO + O \rightarrow X + O_2 \quad (k_5) \tag{85}$$

where the molecule X is a catalyst. As the catalyst is not destroyed, a single molecule can destroy many ozone molecules.

The main catalysts for ozone in the middle atmosphere include reactive hydrogen species or *odd hydrogen* HO_x, reactive nitrogen species and chlorine species. The importance of a given catalyst varies with altitude.

Reactive nitrogen species NO_x play an important role in the mid-stratosphere, while reactive hydrogen species HO_x dominate the catalytic destruction of ozone in the mesosphere, as well as playing an important role in the upper and lower stratosphere. In addition, catalytic cycles involving chlorine species are quite effective in the upper stratosphere, and cycles involving Bromine are quite effective around 20km, both at high latitudes. The role of the Chapman reactions is generally small but is at its greatest in the upper stratosphere.

2.4 Temperature dependence of the ozone mixing ratio

It would be interesting to know how ozone and temperature varies with a passing wave.

Modeling the equilibrium mixing ratio of ozone using only Chapman chemistry gives (Andrews 2000):

$$\mu = \frac{[O3]}{[M]} = \frac{[O2]}{[M]}\sqrt{\frac{j_2 k_2 [M]}{j_3 k_3}} \tag{86}$$

where the square brackets indicate number density, and M is air. The number density of molecular oxygen can be assumed to be approximately 20% of the total air density. If the period of the wave is much longer than the chemical lifetime of ozone, the ozone can be assumed to be in steady state. This is valid for the periods of planetary waves.

The photo dissociation rate coefficients j_i will vary with altitude, but will have a similar dependence on sunlight and temperature, making their ratio relatively constant. The chemical rate coefficients k_i will also have a strong temperature dependence, and can from Table 1-1 and 2-1 in (Sander et al. 2003) be found to be:

$$k_2 = 6.0 \cdot 10^{-34} \cdot \left(\frac{T}{300}\right)^{-2.4} \tag{87}$$

$$k_3 = 8.0 \cdot 10^{-12} \cdot \exp\left(\frac{-2060}{T}\right). \tag{88}$$

By inserting these values, as well as the ratio of the number densities of molecular oxygen and air into equation (86) a crude model of the ozone dependence on temperature can be made.

$$\mu = \frac{[O2]}{\sqrt{[M]}}\sqrt{\frac{6 \cdot 10^{-34}}{8 \cdot 10^{-12}}\frac{j_2}{j_3}\frac{(\frac{T}{300})^{-2.4}}{\exp(\frac{-2060}{T})}}. \tag{89}$$

And the percentage variations in ozone mixing ratio at a given altitude are then found by

$$\mu(\%) = \frac{\mu - \overline{\mu}}{\overline{\mu}} \tag{90}$$

which cancels out the altitude dependent but temperature independent photo dissociation rates j_i.

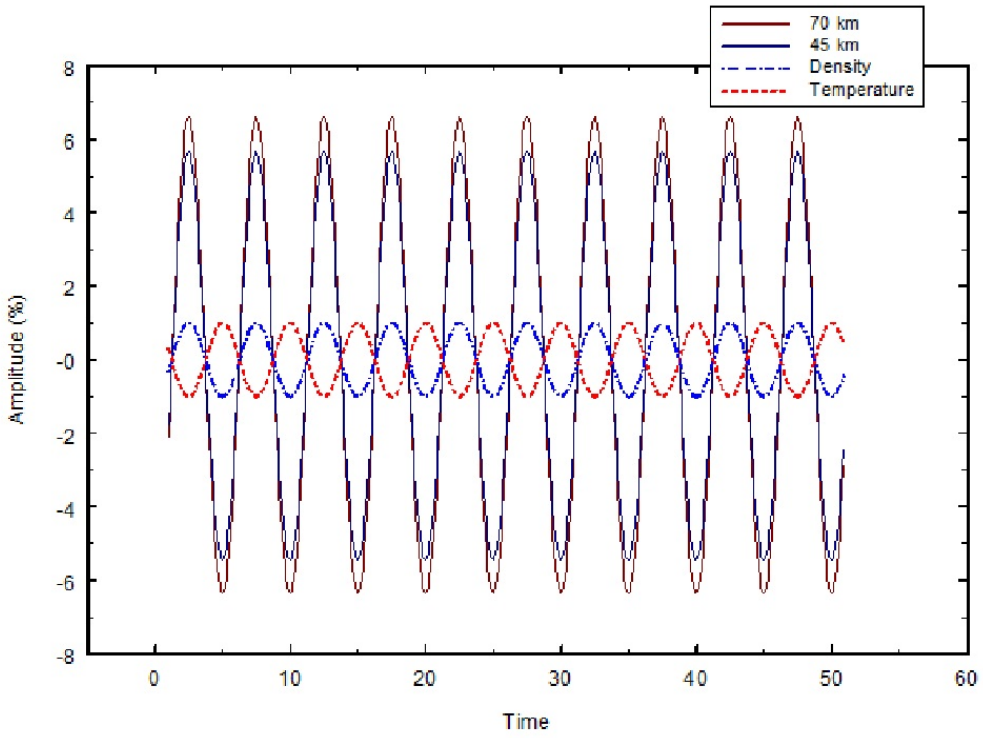

Figure 4: Modeled ozone mixing ratio variation at 45km and 70km due to a 1% temperature variation. From (Kleinknecht 2010)

Kleinknecht (Kleinknecht 2010) calculated these variations for altitudes of 45km and 70km, and found that the ozone mixing ratio percentage variations were six times stronger than the temperature variations, anti-correlated with these and approximately constant with height. See Figure 4.

2.4.1 Using ozone to trace atmospheric motions

The photochemical lifetime of ozone varies strongly with altitude. Though it can have a lifetime of several weeks in the lower stratosphere (Salby 1996), this reduces to only a couple of minutes in the mesosphere, see Figure 5. Below 30km where the ozone column is concentrated, the lifetime is long enough for ozone to be transported by motion, but at higher altitudes this is not the case. Ozone is therefore often considered to be a poor tracer of dynamic motions.

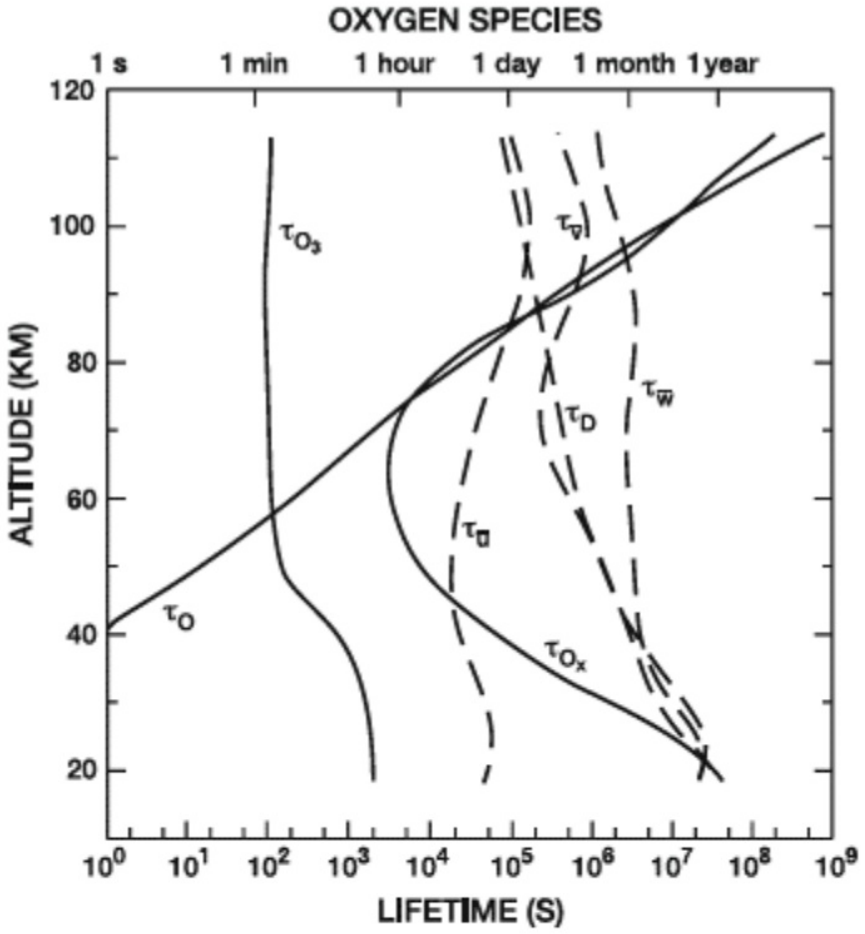

Figure 5: Daytime photochemical lifetimes of O_x, O_3 and O, and characteristic transport lifetimes for mid-latitude winter, from the model of Garcia and Solomon (Brasseur and Solomon 2005)

Due to the short chemical lifetime, a parcel with high mixing ratios of ozone moving through the atmosphere will quickly reduce to the photochemical equilibrium amount in the part of the atmosphere it is moving through, essentially making it a poor tracer. However, mass transport will indirectly affect the ozone, since its chemistry and surroundings will involve longer-lived species that are controlled by transport (Allen et al. 1984).

Therefore, it is still possible to track planetary wave in the ozone mixing ratios. At a given altitude and latitude in an isothermal atmosphere, a wave can be considered as air parcels moving in from above or below the given altitude. In its original location, each air parcel has a temperature T, ozone mixing ratio μ, pressure p and density ρ. If the parcel moves upwards, it expands and cools adiabatically. Since the ozone mixing ratio is dependent on temperature, the ozone mixing ratio will change to adapt to a new steady state ratio different from the original.

Similarly, a sinking air parcel will be compressed, the temperature increases, and the

ozone mixing ratio will adapt to a new steady state. So even though the photochemical lifetime of ozone is too short for it to be considered a good tracer, wave motions will lead to periodic variations in temperature, pressure and density, which in turn affects the ozone mixing ratio (Kleinknecht 2010).

2.4.2 Ozone distribution

Vertical profiles of the ozone mixing ratio show three maxima. The two maxima that were found first are located in the stratosphere and lower thermosphere and are generally known as the first and secondary maxima. Between these two, in the middle mesosphere, a third maximum was later observed at high latitudes during winter. This maximum is known as the tertiary or middle mesospheric maximum.

First maximum The first maximum is the strongest of the three. As mentioned in section 2.3.1, both molecular oxygen and ultra-violet radiation capable of photodissociating molecular oxygen into atomic oxygen is necessary for the production of ozone. The amount of molecular oxygen decreases exponentially with height, while the amount of short wavelength radiation decreases from the top of the atmosphere and downwards. These limitations on molecular oxygen and suitable radiation, combined with photolytic destruction and catalytic cycles destroying ozone lead to a maximum layer of ozone at an altitude of about 20km in tropical regions. From there it is transported to the lower stratosphere in higher latitudes by transport structures such as the Brewer-Dobson circulation.

As the air density decreases exponentially with height, the ozone mixing ratio maximizes at a higher altitude than the ozone density, leading to a maximum in the ozone mixing ratio at altitudes close to 35km.

Secondary maximum The secondary maximum in ozone mixing ratio can frequently be found at altitudes close to 90-95km (Hartogh at al. 2004). Though it can be observed both during the night and the day, it is more prominent at night, as above approximately 60km there is a general increase in ozone during the night. (Allen et al. 1984).

The existence of the secondary ozone maximum is due to the photo dissociation rate of molecular oxygen strongly increasing with height, leading to high concentrations of atomic oxygen in the thermosphere. This concentration decreases rapidly with decreasing altitudes and increasing atmospheric density. However, the atomic oxygen from the thermosphere can be transported down into the region below 100km.

In this region, the three-body reactions (79) and $2O + M \rightarrow O_2 + M$ become more efficient, as they are quadratically dependent on the air density which decreases exponentially with height. Due to the increased efficiency of the three-body reactions, the atomic oxygen is either transformed into ozone or recombined into molecular oxygen, leading to an ozone maximum.

As ozone is depleted by solar radiation, the ozone values are highest during the night. In addition, the secondary maximum vary with vertical winds, which again vary with latitude and time. Due to the pole-to-pole circulation, vertical winds move downward at the winter pole and upward at the summer pole, making the secondary maximum appear at lower altitudes during winter than during summer.

During the night, the ratio of atomic oxygen to atomic hydrogen decides the concentration of ozone. As both the atomic oxygen and atomic hydrogen concentrations are influenced by advective and diffusive transport, the secondary maximum is very variable in both altitude and maximum value (Sonnemann et al. 2006).

The low temperature at the mesopause has been shown to accelerate the ozone production, equation (79), and slow the loss through recombination with atomic oxygen, equation (81), and catalytic interaction with hydrogen, $O_3 + H \rightarrow OH + O_2$ at the secondary maximum (Smith and Marsh 2005). As the temperature increases with altitude in the lower thermosphere, this is an important contributor to the decrease in ozone above the mesopause, together with the decreased efficiency of the three-body reactions with height.

Tertiary maximum The tertiary maximum, or *middle mesospheric maximum* as it is sometimes called, was the last of the three maxima to be found, explaining why it was named the tertiary maximum even though it is found between the other two. It can be found during the night at high latitudes, just equatorward of the polar night terminator in the winter mesosphere, usually at altitudes of approximately 72km (Sofieva et al. 2009).

The tertiary maximum is clearly separated from the secondary maximum by a region of very low ozone mixing ratios around 80km, indicating that the tertiary maximum does not result from transport of ozone from the secondary maximum but is the result of local effects (Sonnemann et al. 2006).

The maximum is created by a large decrease in the destruction of ozone, without a matching decrease in production. As mentioned in the chapter on catalytic cycles, the most important catalyst for mesospheric ozone is odd hydrogen, HO_x.

The primary source of odd hydrogen is the photolysis of water vapour, which requires ultra violet radiation with wavelengths shorter than 185nm. The production of odd oxygen from molecular oxygen also requires photolysis, but by radiation with longer wavelengths than that necessary for the water vapour.

At high latitudes, the solar zenith angle is large and incoming sunlight has to pass through more of the atmosphere, giving large optical depths for these latitudes. This leads to a sharp attenuation of the short wavelength radiation necessary to create odd hydrogen, while the longer wavelengths necessary for odd oxygen production are attenuated more slowly.

The relatively large decrease in ozone destruction following from the decrease of odd hydrogen is therefore not matched by a similar decrease in the odd oxygen production, leading to a local ozone maximum (Marsh et al. 2001).

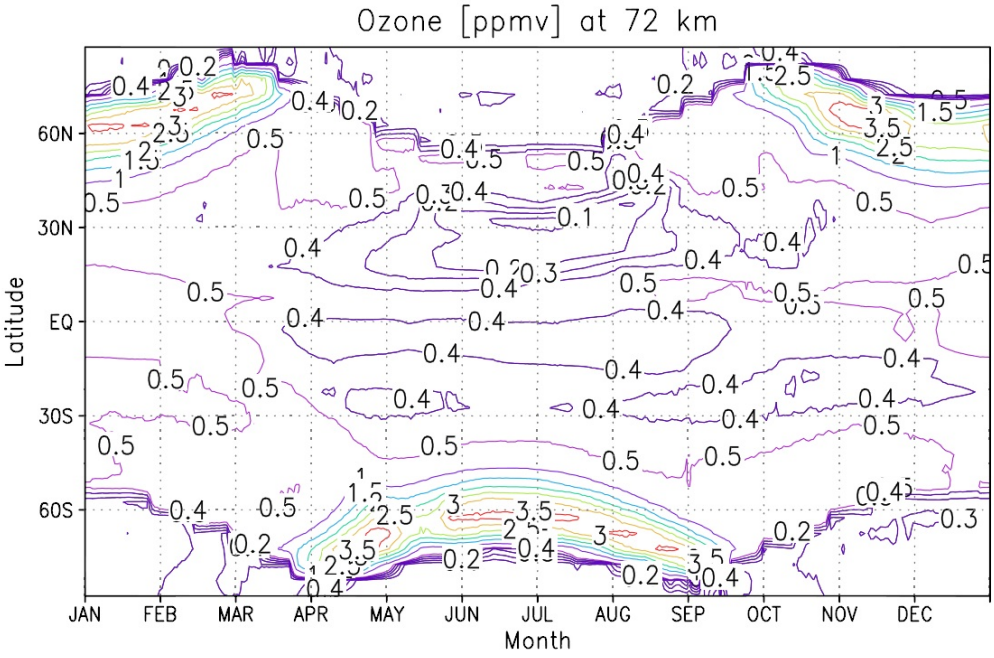

Figure 6: Contour plot of the midnight ozone mixing ratios depicted in a latitude-season section at 71km altitude, showing the arcs of the tertiary ozone maximum close to the polar night terminator. From (Sonnemann et al. 2006)

The tertiary ozone maximum has been seen to be strongly modulated by planetary scale oscillations, in addition to being strongly influenced by stratospheric warmings and energetic particle precipitation events (Sonnemann et al. 2006; Sofieva et al. 2009).

Annual variations of the ozone concentrations in the tertiary ozone maximum have been measured. Measurements show that the annual maximum is found some time before the winter solstice, followed by a relative minimum during January and February in the Northern hemisphere. Another, somewhat smaller maximum then appears around the spring equinox followed by the absolute minimum during summer (Sonnemann et al. 2007).

2.5 Detection of ozone through millimeter wave remote sensing

As mentioned in the introduction, there are several different methods for measuring atmospheric constituents. Here, the ground-based millimeter wave remote sensing used to find the ozone profiles will be described. Ground based measurements of the millimeter wave range are especially suitable for measuring changes in ozone concentration, as they are only weakly dependent on weather conditions, and are able to detect signals with a high resolution (Kuntz et al. 1997).

Ground-based millimeter wave remote sensing works by measuring line spectra of emit-

ted radiation from the atmosphere. The emission lines from ozone and other molecules are due to molecules being able to absorb and emit certain quantized amounts of energy, equal to the difference between energy levels in the molecule. These energy quanta correspond to radiation at wavelengths characteristic for the molecule, and were discussed in more detail for the diatomic hydroxyl molecule in section 2.2.1.

Molecules can be thermally excited to higher states by collisions with other molecules. When these excited molecules radiate away their excess energy, the radiation can be measured from the ground. The resulting line spectra will contain lines from many different atmospheric constituents, which can be identified by the characteristic wavelength of their emissions.

However, the lines in the line spectra are not truly discrete lines. Rather, they occupy bands of wavelengths, mainly due to Doppler- and pressure broadening, in addition to natural broadening of the line width. These effects are described in (Salby 1996):

Natural broadening is a result of the uncertainty of energy in the different states involved in the the transition leading to the emission. For the millimeter-wave spectroscopy used to find ozone profiles, natural broadening is insignificant compared to Doppler- and pressure-broadening.

Molecular motion along the line of sight leads to a frequency shift for the emitting molecules, and further *Doppler-broadening* of the spectral line. The frequency shift is

$$\nu = \nu_0(1 \pm \frac{v}{c}) \tag{91}$$

where ν_0 is the frequency at the line center. This, combined with the Boltzmann probability distribution

$$p(v) = \sqrt{\frac{m}{2\pi k_B T}} \exp\left(\frac{-mv^2}{2k_B T}\right) \tag{92}$$

where m is the molecular mass and k_B the Boltzmann constant, gives a shape factor

$$f_D(\nu - \nu_0) = \frac{1}{\alpha_D \sqrt{\pi}} \exp\left[-\left(\frac{\nu - \nu_0}{\alpha_D}\right)^2\right] \tag{93}$$

where $\alpha_D = \frac{\nu_0}{c}\sqrt{\frac{2k_B T}{m}}$ is the Doppler half width divided by $\sqrt{\ln 2}$. The shape factor f_D describes the width of a spectral line due to Doppler broadening.

Pressure broadening or *collisional broadening* is due to collisions with other molecules. It will therefore depend on the density in the area the radiation is emitted from, and will change with altitude. This line broadening is what allows the identification of the altitude of an emitting molecule.

In the same way Doppler-broadening was modeled by the Doppler line shape, pressure broadening will be modelled as the Lorentz line shape

$$f_c(\nu - \nu_0) = \frac{\alpha_c}{\pi(\nu - \nu_0)^2 + \alpha_c^2} \tag{94}$$

where $\alpha_c = \alpha_0 \left(\frac{p}{p_0}\right) \left(\frac{T_0}{T}\right)^{\alpha}$ is the collisional half-width, with $\alpha_0 \cong 0.1\text{cm}^{-1}$ being the half-width at standard temperature T_0 and pressure p_0. The collisional half-width is inversely proportional to the mean time between collisions, and the exponent α depends on the gas experiencing the collisional broadening. For ozone it is approximately 0.76 (Brasseur and Solomon 2005).

In the troposphere and lower stratosphere, line broadening is mainly due to collisions between molecules. These collisions become less frequent at very high altitudes, where the Doppler broadening begins to dominate. In the region in-between, both broadening processes contribute. If they are assumed to be independent, they can be combined into the *Voigt profile*, which is a good approximation to observed line shapes. An example of Lorentz-, Doppler- and Voigt line shapes can be seen in Figure 7

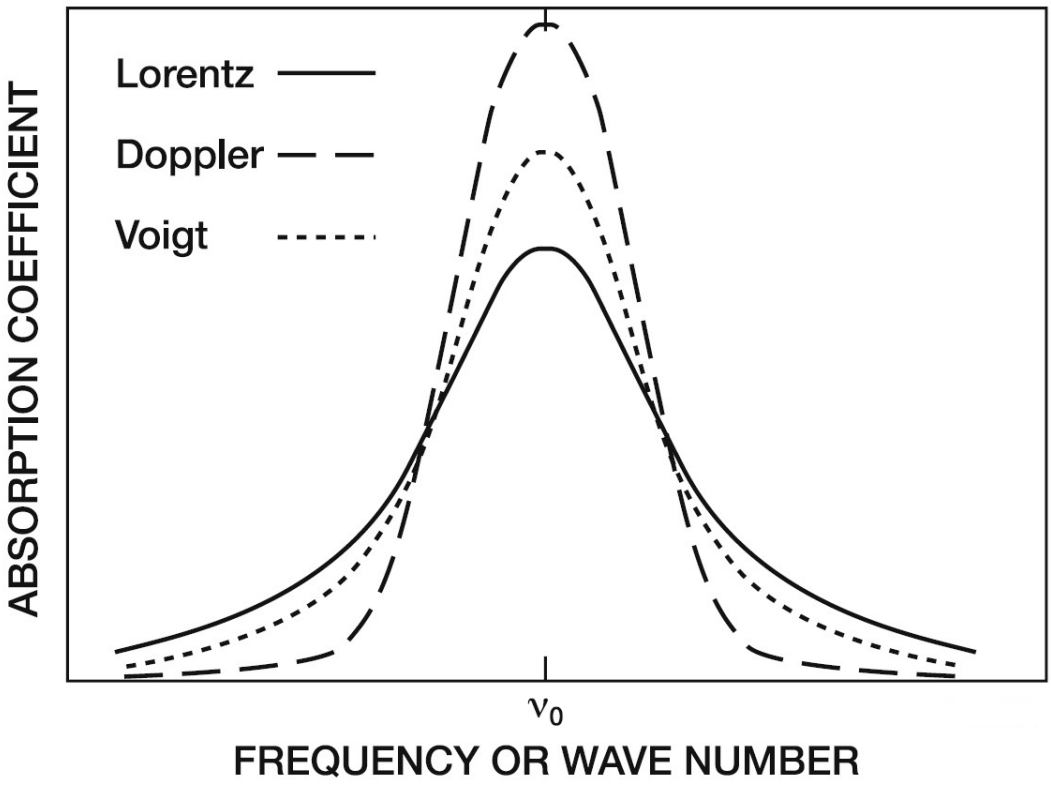

Figure 7: Lorentzian, Doppler and Voigt spectral line profiles for approximately equal half widths and intensities, from Andrews et al. 1987, found in (Brasseur and Solomon 2005)

As mentioned, the pressure broadening is due to collisions with other molecules, and the shape of the spectral line due to pressure broadening will depend on the density of the surrounding air. The line width varies linearly with pressure, and since the pressure decreases exponentially with altitude it is possible to find the altitude at which the radiation was emitted by looking at the line width.

At high altitudes the time between each collision increases, and the spectral line resulting from radiation in this area will be narrower than one originating at lower altitudes. By observing these lines from the ground, one will see the sum of spectral lines emitted at all altitudes above the observation point. Each component of this sum will contribute to the total line spectrum relative to the amount of molecules emitting at its altitude of origin.

To find how much each component of the line spectrum contributes to the total, a model containing all components can be fitted to the measured spectrum by varying the contribution of each component. Due to noise and possible measurement errors, it is not possible to find an exact, unique solution. Approximate solutions can however be found, and to control the fitted spectra an a priori profile can be used. For more details on how to estimate the state of the atmosphere from measurements of emitted thermal radiation, see (Rodgers 1976).

3 Data and instrumentation

Two datasets were used in this thesis, a set of temperature data from an altitude of 87km and a set of ozone measurements ranging in altitude from ground level to 106km.

3.1 Temperature data

The temperature data was obtained by a scanning Michelson interferometer at the British Antarctic Survey station at Rothera (67°34′S, 68°08′W). The interferometer measures hydroxyl airglow. Since hydroxyl is found in a thin layer at a height of 87km and the low-lying rotational levels of the OH Meinel (3,1) band nightglow are in thermal equilibrium with its surroundings (Pendleton et al. 1993), we can find the temperature at this height from the measurements.

The dataset includes day of measurement, radiance, error in radiance, temperature, error in temperature and number of measurements per night for each year from 2002 to 2009 for both the OH Meinel (3,1) and (4,2) bands. In this thesis, only the day, temperature and error in temperature data for 2009 are being used, and only from the OH Meinel (3,1)-band.

When the sun is up, the radiance from hydroxyl can not be distinguished from that of sunlight with the same frequency, so measurements can only be made at night. In addition, the sunlight decreases the amount of ozone in the atmosphere, which again decreases the concentration of hydroxyl. As the sun is up most of the day during the Antarctic summer, the dataset has large gaps for these months. In addition, cloudy nights or instrument down time give smaller gaps at other times of the year.

3.2 Ozone data

The ozone measurements used were obtained at the Norwegian Polar Institute's Troll research station at the Antarctic Plateau (72°1′S,2°32′E). The measurements were found using the ARON (Antarctic Radiometer for Ozone and Nitric oxide) microwave radiometer. The ARON was developed as part of the Sun Earth Connection programme at the British Antarctic Survey, and is as previously mentioned placed at the Troll Research Station. The placement of the instrument is due to the measurements requiring a dry atmosphere to minimize water vapour absorption. The Troll Research Station is located in a desert 235 kilometers from the coast, at an altitude at 1270m above mean sea level (NPI 2006) where the climate is cold and dry. The location and 30° elevation viewing angle of the instrument gives an atmospheric transmission of $> 65\%$ (Espy et al. 2006).

ARON detects nitric oxide, ozone and carbon monoxide by observing several different spectral lines in the region around 230-250GHz.

More information about the design of ARON can be found in (Espy et al. 2006).

4 Analysis

The purpose of the analysis done in this thesis was to find and isolate planetary waves in ozone and temperature data, in order to be able to describe the waves present in the middle atmosphere above Antarctica during 2009, and how they develop with time and altitude.

Both of the datasets used originally consisted of several measurements per night. To prepare for the analysis, uncertain and skewed measurements were removed from the datasets, which were then averaged to give only one value per night per dataset. These values where then used in the further analysis.

4.1 Averaging of temperature data

The average temperature for each night was found using

$$\langle T \rangle = \frac{\sum_{i=1}^{N} \frac{T_i}{(\delta T_i)^2}}{\sum_{i=1}^{N} \frac{1}{(\delta T_i)^2}} \tag{95}$$

where T_i are the individual measurements and δT_i is the uncertainty of each measurement. All nights with 10 or fewer measurements were removed from the dataset before averaging to avoid uncertain measurements skewing the average. The standard error of this mean value was then found by

$$\Delta T = \left(\frac{1}{\sum_{i=1}^{N} \frac{1}{(\delta T_i)^2}} \right)^{\frac{1}{2}} \tag{96}$$

These are the weighted mean and the standard error. In the weighted mean, each temperature-value has a weight $\frac{1}{(\delta T_i)^2}$, making very uncertain measurements contribute less to the weighted mean than more certain measurements. The reason for using the standard error instead of the standard deviation is that for a signal containing some wave activity, the standard deviation would be a measure of the wave amplitude rather than the uncertainty of the mean.

If all the uncertainties δT_i were the same, each temperature-value would contribute equally, and the equations would reduce to the arithmetic mean and $\Delta T = \sqrt{\frac{\delta T}{N}}$, which is the usual formula for the standard error, with δT being the standard deviation in this hypothetical case.

The averaging over each night was done before this thesis was started, and it is the nightly averaged values that have been used throughout the thesis.

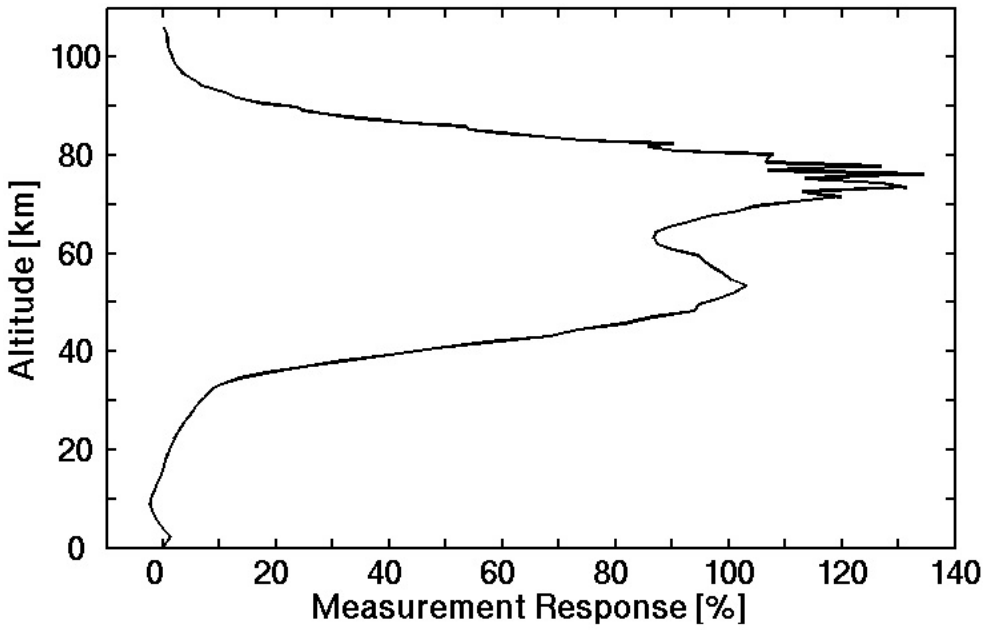

Figure 8: Measurement response for an inversion in January 2009, from (Kleinknecht 2010)

4.2 Solar elevation and averaging of ozone data

The altitude profiles in the ozone dataset range from ground level to 106km of altitude. However, these are based on both measurements and a priori profiles. To see at what altitudes the ozone profiles represent the measurement and where they mainly reflect the a priori profile, the measurement response (MR) can be used. As shown in (Kleinknecht 2010), each altitude has a unique measurement response, but they all have a measurement response of more than 30% for the region between 35km and 75km. In this region there is enough information for the a priori profile to be adjusted, meaning that it is possible to extract the real ozone profile. Outside of this altitude interval, the information given from the dataset will mostly contain a priori information, with variations mainly being caused by noise. Therefore, only data from the region between 35km and 75km of altitude will be used. A sample measurement response can be seen in Figure 8.

As seen in the chapter on ozone-theory, section 2.3.1, the mixing ratios have large diurnal variations due to sunlight strongly influencing the production and destruction of ozone. The ozone data is in the form of hourly averages, given for the period between December 2008 and November 2009, usually with a pause of about 2 hours in the middle of the day due to the observation schedule of the instrument. In order to avoid using data influenced by photo dissociation from sunlight, the solar elevation was found for the time and location of each measurement. The location was Troll Research Station, at 72°1′S and 2°32′E for all the measurements.

To find the solar elevation at a given time for this point, the Matlab file *Solar Azimuth and Elevation Estimation* by Darin Koblick was used, (Koblick 2009). Then all mea-

surements with a solar elevation higher than $-10°$ were removed from the dataset. This means that the first usable measurement appears during the first night of March, and the last in the middle of October 2009.

For each night with usable measurements, the measurements were averaged, giving only one value per night. During the Antarctic winter the solar elevation is below $-10°$ most of the time, giving many usable measurements per night to be averaged. Fewer measurements have an acceptably low solar elevation during the spring an autumn, and during the Antarctic summer the sun stays above the horizon most of the time. Even though it occasionally moves below the horizon, the sun is always found above the $-10°$ limit in summer, giving no usable measurements from this season. However, each of the hourly measurements is already an average of 112 spectra, so even nights with only one acceptable measurement can still be used in the further analysis.

4.3 Removing seasonal variations

During the year there will be seasonal variations to the temperature and ozone mixing ratios that are not caused by atmospheric waves. Since only periodic motions with periods varying from approximately 2 to 50 days are of interest, the long period seasonal variations should be removed.

One way of doing this is to subtract a description of an "average year" without atmospheric waves or other disturbances. This seasonal fit would consist of low-frequency periodic motions fitted to resemble an average year. However, as the amplitudes of atmospheric motions generally increase with increasing altitude, it would be necessary to fit a different set of amplitudes for each altitude of the data. As the ozone dataset alone consists of data from 41 different altitudes, even after the areas dominated by a priori profiles have been removed, this would be unnecessarily time consuming.

Instead, a high-pass filter was applied to all the datasets in order to filter out low frequency motions, while leaving periodic motions with higher frequencies as unchanged as possible.

Before the filter could be applied, the data had to be interpolated, to get sets of evenly sampled data that the filter could be applied to. This was especially important for the temperature data, which had several gaps and missing nights due to cloudy weather and instrument downtime. The ozone datasets were almost complete, lacking only one night of measurements. The interpolation was done using the *cubic spline* interpolation method in Matlab, resulting in an evenly sampled temperature time-series ranging from night 34 to night 264 of 2009, and similarly evenly sampled ozone data ranging from night 60 to 286 of the same year.

To remove the low frequency seasonal variations, a Butterworth IIR high-pass filter was used. The Butterworth filter was chosen since it is designed to have a maximally flat frequency response in the chosen passband. The price for getting a flat frequency response in the passband is that the roll-off becomes slower, but since the frequencies of the seasonal variations are much lower than the frequencies of the interesting at-

mospheric waves, a flat frequency response in the passband was seen as more valuable than a steep roll-off.

The end of the stop-band, w_{stop}, and start of the pass-band, w_{pass}, for the highpass filter were given as normalized frequencies. Normalized frequencies are values between 0 and 1, with 1 corresponding to the Nyquist frequency of a dataset the filter is applied to. As both of the datasets have been averaged to one value per night, they have a Nyquist frequency of $f_N = \frac{f_S}{2} = \frac{1}{2}$ day^{-1}. Since one day is the natural time unit to use when looking at atmospheric waves, normalized frequencies seem to be a more natural choice than frequencies given in Hertz.

It was decided that all periodic motions with periods longer than 80 days should be completely removed, placing the end of the stop-band at a normalized frequency of $w_{stop} = 0.025$. As all periodic motions with periods shorter than 30 days should be completely included, the start of the pass-band was placed at the normalized frequency $w_{pass} = 0.0666$. These two values give a fourth-order Butterworth filter with a normalized cut-off frequency of 0.047978.

Ideally, the filtered data should have a phase shift as close to zero as possible. This can be attempted by filtering the data more than once, first in the forward time direction and then in reverse. Also, in recursive filters, the output at a given time is found using previous inputs and outputs, which leads to transient errors at the beginning of the time range where few or no previous outputs are available (Kormylo and Jain 1974).

To perform the zero-phase digital filtering, the *filtfilt*-function in Matlab was used. This function processes the input in the forward and reverse direction, and minimizes the transient errors at the beginning and end of the dataset by matching initial conditions. However, some transient errors still persist, and seem to increase with increasing filter order n. The filter order using *filtfilt* is twice that specified for the filter the function is used with. To avoid large errors at the beginning and end of the dataset the order of the Butterworth filter was therefore kept as low as $n = 4$. As mentioned, the frequencies of seasonal variations are much lower than those of the interesting atmospheric waves, so the slow roll-off given by the low filter order was still seen as acceptable.

In the stopband, the filter was set to attenuate the signal by 20dB, while fluctuations of up to 0.3dB in the frequency magnitude response were allowed in the passband.

After applying this filter to all the data, the filtered data was plotted to show the remaining variations throughout the year.

When plotting variations in temperature and ozone mixing ratio in the same plot, one has to correct for the different units of the measurements. Unadjusted, the temperature values would completely drown any contributions from the ozone data. In order to avoid this, the percentage variations were used instead of the original.

Each ozone measurement was divided by the mean value of the mixing ratio, giving the variations as percentages of the mean value. Similarly, each temperature measurement was divided by the mean of all temperature measurements. The resulting plot can be seen in Figure 12.

It should be repeated that since the ozone data from above 75km mostly reflected the a priori model, no ozone data was used above this limit. Because of this, the contour lines in the area between 75km and the temperature data at 87km are based on the data at these two altitudes.

4.4 Finding frequencies

In order to find the frequencies dominating the non-seasonal variations, the Lomb normalized periodogram was calculated for each altitude of the filtered data.

The Lomb periodogram is normally used to perform spectral analysis on unevenly sampled data where normal Fourier transforms are unsuitable (Press and Rybicki 1988). Here, it will be used on data that has been interpolated and thus appears to be evenly sampled. The reason for using this method on evenly sampled data is that the data contains large amounts of noise and random variations. The Lomb method not only gives the normalized periodogram but also includes the statistical significance for each value of the periodogram. It therefore makes it easy to quickly find the probability of a given peak belonging to an actual signal or just consisting of noise.

In theory, the Lomb method first computes the data's mean and variance

$$\overline{x} = \frac{1}{N}\sum_{i=1}^{N} x_i \tag{97}$$

$$\sigma^2 = \frac{1}{N-1}\sum_{i=1}^{N}(x_i - \overline{x})^2 \tag{98}$$

Then, for each frequency, the angular frequency $\omega = 2\pi f$ is found, and a time offset τ is computed. This is defined by the relation

$$\tan(2\omega\tau) = \frac{\sum_j \sin(2\omega t_j)}{\sum_j \cos(2\omega t_j)} \tag{99}$$

The Lomb normalized periodogram is then defined by

$$P_N(\omega) \equiv \frac{1}{2\sigma^2}\left\{\frac{[\sum_j (x_j - \overline{x})\cos\omega(t_j - \tau)]^2}{\sum_j \cos^2\omega(t_j - \tau)} + \frac{[\sum_j (x_j - \overline{x})\sin\omega(t_j - \tau)]^2}{\sum_j \sin^2\omega(t_j - \tau)}\right\} \tag{100}$$

This gives the spectral power as a function of angular frequency ω, while the time offset τ makes $P_N(\omega)$ independent of a possible shift of all the t_j's by a constant (Press et al. 1992).

Since the data is sampled once per night, the Nyquist critical frequency is $f_N = \frac{f_s}{2} = \frac{1}{2}\text{day}^{-1}$, as previously mentioned. Up to this frequency, the dataset contains complete

information about all spectral components of signals. The dataset can contain scrambled or aliased information about components with higher frequencies, but because of this limit, only wave motions with periods of 2 days or more will be considered as possible atmospheric waves.

To find the Lomb normalized periodogram for each altitude, the Matlab implementation created by Saragiotis is used (Saragiotis 2008). All the normalized periodograms are put together to create a contour plot with contour lines signifying peaks that have a 50%, 10%, 5%, 1%, 0.5% and 0.1% probability of being noise.

4.4.1 Finding more frequencies

Something worth noticing about the Lomb normalized periodogram is that the significance levels are decided by the highest peak. If the analyzed data consists of a single sine-wave, the standard deviation would be $\sigma = A * 0.707$, where A is the peak amplitude of the wave, half of the peak-to-peak amplitude. If the data contains more than one wave, waves with small amplitudes can be interpreted as noise by the Lomb normalized periodogram, since they are small enough to vanish among the normal variations of the largest-amplitude wave.

So if one peak strongly dominates, other significant frequencies might be dismissed as likely to consist only of noise. To make sure no peaks are lost due to this effect, new significance levels are calculated as they would be if the highest peak was filtered out. This leads to some small changes at high altitudes in the contour plot, but the five main bands are still visible and the rest of the plot mainly unchanged.

The resulting plot can be seen in Figure 9. For a comparison of the original Lomb normalized periodogram and the one with significance levels calculated from the second highest peak, see the appendix Plots, where the two plots can be found in Figure 17 and 18.

In the contour plot displaying the Lomb normalized periodograms for the different altitudes, it can be seen that certain frequency intervals contain peaks that appear more or less consistently at several different altitudes. From this plot it appears that the middle atmosphere above Antarctica during the period from March to the middle of October 2009 contained five or more oscillations that might be planetary waves.

Looking closer at the frequency intervals, there seem to be oscillations with periods of 14-15 days, 17-20 days, 21-23 days, and one or more with periods between 25 and 45 days. Also, an oscillation with a period of 11-12 days appears to exist, but the frequency of this one is only statistically significant at the lowest of the altitudes.

However, the four other frequency bands are still strong enough to influence the significance levels into hiding other weaker, but still significant peaks. In order to check this, each of the five main peaks is in turn filtered out, and the periodograms found anew to look for new frequencies. By filtering out all the five frequency bands found in the original periodograms, three new frequencies are found. These correspond to periods of 4, 5 and 8.5 days and are found consistently at more than one altitude with significance

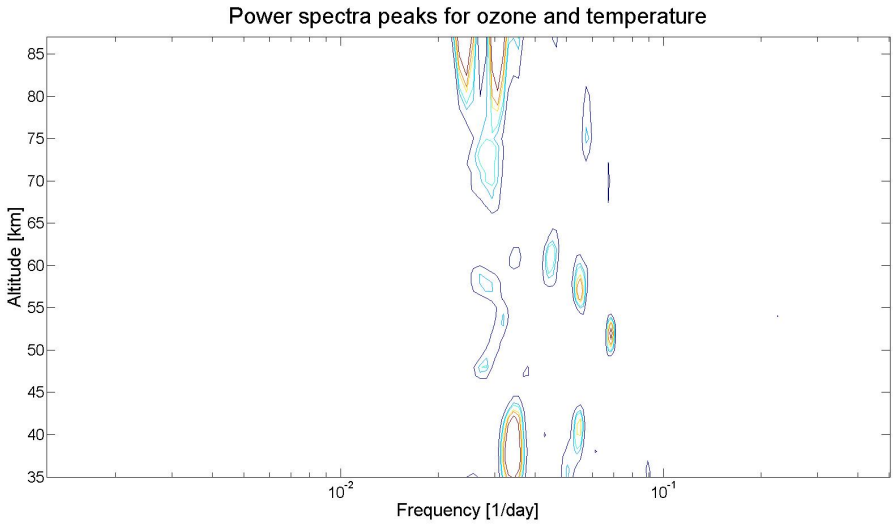

Figure 9: Lomb normalized periodograms, with significance levels decided by the second highest peak. The contour lines indicate 50%, 10%, 5%, 1% and 0.5% chance of being caused by noise.

levels of 50% or higher. In addition, the 11-12 day wave motion turns out to consist of not one, but two separate but still close frequencies, and can now be found at several altitudes, not only at the very lowest ones. Further filtering does not reveal any new significant frequencies after this.

4.5 Isolating interesting frequencies

In order to look closer at the oscillations found from the Lomb normalized periodogram, each of the nine frequency intervals were in turn isolated using a bandpass-filter. The lowest frequency interval is very wide and might contain several different oscillations, or a superposition of such.

The analyzed frequency intervals and their approximate periods can be found in Table 2.

In order to isolate each frequency, a Butterworth bandpass filter allowing each specific frequency interval to pass was used on the original ozone and temperature datasets. The Butterworth filter was again chosen for its flat response in the stop- and passbands. Since there is some space between each interesting frequency interval the slow roll-off is still acceptable, though some attenuation in the stopband was sacrificed to keep the roll-off reasonably steep even for the quite low filter orders necessary to avoid large errors at the beginning and end of the filtered datasets.

Table 2: Interesting frequency intervals

Interval#	Frequency interval	Period [days]
1	0.2510-0.2550	4
2	0.1912.0.1949	5
3	0.1164-0.1189	8.5
4	0.07910-0.08887	10-11
5	0.08152-0.08960	11-13
6	0.06740-0.06863	14-15
7	0.05009-0.05760	17-20
8	0.04204-0.04657	21-24
9	0.02206-0.0380	26-45

4.6 Analyzing the isolated frequency intervals

After having found and isolated nine frequency intervals that seemed as though they might contain planetary waves, each frequency interval was in turn subjected to the same analysis:

The filtered data was plotted against time and height to see how the remaining percentage variations in ozone and temperature vary during the year and at different altitudes. Again, the percentage variations were used instead of the raw filtered data in order to avoid the temperature measurements completely dominating the resulting plots.

In addition, percentage of ozone mixing ratio variations are expected to be anti-correlated with, and six times stronger than the temperature variations. This is described in more detail in section 2.4. To make any vertical propagation by planetary waves more easily visible in the contour plots, the temperature-variations have therefore been multiplied by -6 before they were plotted. These plots can be found in the Results-section of the appendix Plots.

Since each interesting frequency interval has some width to it, it would be interesting to see if the remaining variations in ozone and temperature were dominated by a specific frequency within the interval, whether this or these frequencies vary with altitude, and whether frequencies outside of the chosen interval still influence the remaining variations. It would be especially interesting to see if there are differences between the altitude interval 35-75km and 87km, since the ozone and temperature data might react differently to passing planetary waves.

In order to see which frequencies that can still be found in the filtered datasets, the Matlab-function *periodogram* was used for each altitude. This returned an estimate of the power spectral density of the dataset at that altitude, in decibels per unit frequency, and a corresponding vector of frequencies ranging from zero to half the sampling frequency. These periodograms were once again plotted together to give a contour plot, showing power spectral density as a function of frequency and altitude.

As before, the difference in scale leads to the temperature data completely drowning out the ozone, so each periodogram from the ozone data had to be divided by the mean

of all the ozone periodograms, and the periodogram from the temperature was divided by its own mean, giving percentage changes.

The contour plots of power spectral density relative to the mean for each data type, and as a function of frequency and altitude can again be found in the Results-section of the appendix Plots, together with the variations throughout the year.

5 Results and Discussion

Finding the Lomb normalized periodogram for each of the 41 ozone datasets and the one temperature dataset and plotting them together resulted in contour plots showing peaks with more than 50% probability of not being caused by noise, plotted as a function of frequency and altitude. An example of this, with no dominant peaks removed, can be seen in Figure 9

Nine frequency intervals containing consistent, significant peaks appeared. These intervals contained wave motions with periods of 4, 5, 8.5, 10-11, 11-13, 14-15, 17-20, 21-24 and 26-45 days. Each of these intervals was isolated, filtering out all other periodic motions. The variations and power spectra for each of the wave motions can be found in the Results-section of the appendix Plots, in Figure 21 to 38. Interesting plots will be used in this chapter to illustrate points relevant to the discussion of the results, but they can still be found in the appendix, to keep them all collected in one place and presented in order of increasing wave period.

5.1 Consistency of the isolated wave structures

The first interesting point to look at is whether the filtered frequency intervals contain the expected wave motions. This can be seen most clearly from the power spectra, which show the dominating frequencies at each altitude.

For most of the isolated motions, the power spectra are dominated by the single expected frequency which is more or less the same for all altitudes. It does disappear at certain altitudes between 40km and 60km, which is probably due to strong wind fields at these altitudes, but will be discussed in more detail later.

Though most of the power spectra are quite clearly dominated by a single frequency, additional, weaker frequencies can sometimes be seen. For example, both the 14-15 and 17-20 day waves appear to have a weak additional peak at a somewhat lower frequency at 87km, and another weak frequency peak can be found at low altitudes for the 4-day wave.

In addition, both the 11-13 and 26-45 day wave motions have more than one dominating frequency at certain altitudes. For the 11-13 day oscillation, the power spectra seem to be dominated by two frequencies at low altitudes. This might either be two separate waves, or that the frequency has changed with time.

The power spectra give no information about the time when the oscillations take place, so only information about the entire year can be extracted from these. If an oscillation originally was dominated by a specific frequency, but this frequency later shifts to a new value, it might show up as two separate peaks. If the power spectra could be seen as a function of time as well as altitude, it might be possible to discern whether there actually are two oscillations, or just one whose frequency gets shifted at low altitudes during the year.

The other oscillation dominated by more than one frequency is the long 26-45 day motion, see Figure 10. It appears to be dominated by two main frequencies at low altitudes, but the highest of these disappears completely close to 50-55km, and does not reappear again before the temperature data at 87km. The other dominating frequency shifts strongly with altitude, almost overlapping the first, and generally twists and turns. In short, this oscillation is much less clear than the shorter period ones, and might not even be a single oscillation at all.

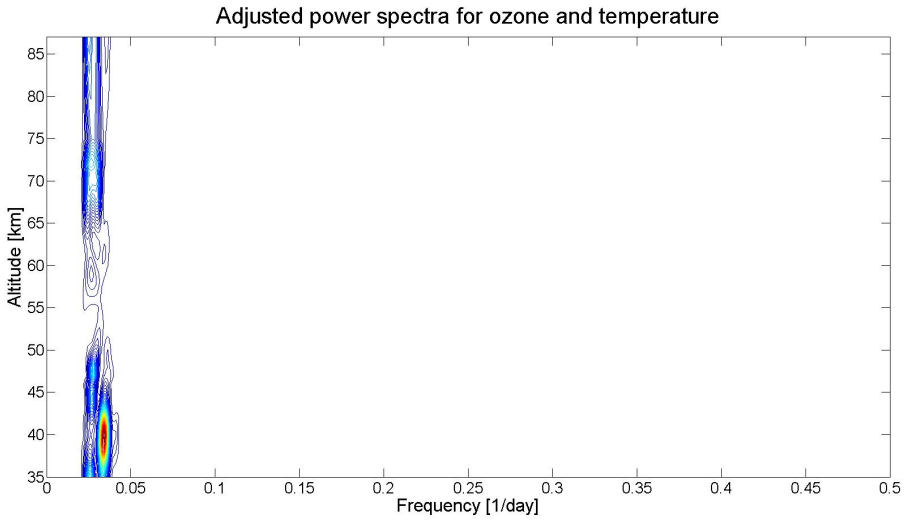

Figure 10: Power spectra for 26-45 day wave motions. In order to make both datasets visible, values from 35-75km have been divided by the mean of all values for ozone, and values at 87km by the mean of all values for temperature.

Though the 26-45 day interval does contain frequencies strongly dominating the non-seasonal variations, and at times does appear to have some sort of planetary wave structure, it varies strongly both with time and altitude and breaks down almost completely during the Antarctic spring. It might be that this is a superposition of several shorter-period waves.

In addition to the power spectra, for most of the oscillations the plots of variations with time for all altitudes can also be seen to contain consistent wave structures more or less all the way from 35 to 87km. They do however contain bands at specific altitudes where the variations either shift to one of the sides, or entirely disappear before continuing again once they get above the band. It should be noted that the area between 75 and 87km is based solely on the values at these two altitudes, since ozone data from this area would mostly reflect a priori models and was therefore not included in the analysis.

5.2 Fit between ozone and temperature data

For all the isolated wave motions, the periods of the waves observed in the ozone up to 75km and in the temperature data at 87km are more or less consistent. Not only do the rough periods coincide, but they also develop similarly with time.

The 17-20 day oscillation has a point just before midwinter when the period of the waves increases temporarily. The 14-15 day oscillation has a gradual increase in wave period with time, moving from closer to 14 days to closer to 15 days. And the two longest period waves both appear to get gradually get shorter wave periods with time, though it is difficult to say for sure in the case of the 26-45 day wave where the time before midwinter is the only time-interval with more or less consistent wave structures.

All of these changes are found both in the ozone data at 75km and in the temperature data at 87km. Though there is some variability in the exact period of a wave at a given time for the two altitudes, this is no more than the variability between ozone data at different altitudes. Therefore, the waves found in the two different datasets seem to be in agreement.

In most of the variations, there is a phase shift between the ozone data at 75km and the temperature data at 87km. This is not surprising, as they are measured from different stations. The ozone data is measured from Troll (72°S,2°E) and the temperature data from Rothera (68°S, 68°W), with a distance of approximately 2500km between them. The zonal distance between the two stations will lead to one of the datasets lagging or leading the other. The exact amount of this lag will depend on the zonal velocity of each wave.

The exact connection between wave variations at 75 and 87km, shown in the variation-plots, cannot be trusted to correct, as Matlab automatically will try to connect the two points in the variation that appear to be the closest. If there is a large lag between the two stations, two consecutive wave maxima or minima might be connected, reducing the total amount of lead or lag, but giving an erroneous impression of the amount one measurement is lagging or leading the other.

5.3 Identification of normal modes

In previous work done on planetary waves, some waves have been found more frequently than others. Table 2.1.6 in section 2.1.6 showed some common westward propagating or westward traveling waves in the middle and upper atmosphere.

The 4-day wave might be the (2,1) Rossby first symmetric normal mode with zonal wave number s = 2, and the 5-day wave might be the (1,1) Rossby first symmetric normal mode, with zonal wavenumber s = 1. Both these waves are normal modes traveling westward with the atmosphere, having no change of amplitude with height. From the plots of variations in percentage ozone mixing ratio and temperature found in the analysis, this seems reasonable for both of these waves. There are variations with altitude, but these appear to vary with the ozone mixing ratio or other changes rather than continuously increasing with height. See for example the plot of percentage variations for the 5-day wave, seen in Figure 11.

Both the 4-day and 5-day wave have been reported frequently, among others in (Forbes 1995), (Hiroata and Hirooka 1984) and (Salby 1981). The 5-day wave was also reported in (Randel 1992).

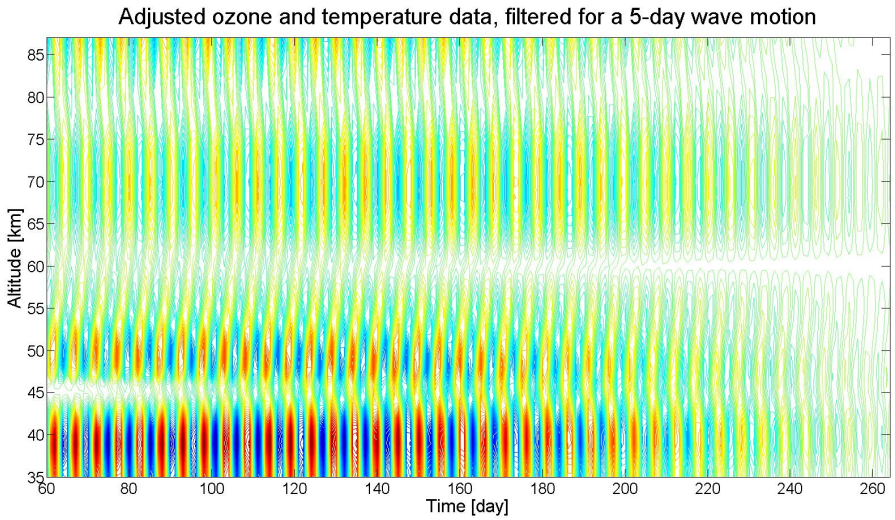

Figure 11: Percentage variations in ozone and temperature for the 5-day wave. The temperature data at 87km has been multiplied by -6 to make the waves more visible at this altitude. The amplitude of the variations does not increase with increasing altitude, which is as expected for a normal mode.

It was shown in section 2.1.6 that eastward zonal winds could Doppler-shift the frequencies, leading to periods longer than those of the ideal case. Therefore, both the 10-11 and/or the 11-13 day oscillations might be the quasi 10-day first antisymmetric normal mode (1,2). Similarly, the 17-20 day oscillation found might be the quasi 16-day second symmetric (1,3) normal mode.

The remaining 8.5-, 14-15, 21-24 and 26-45 day oscillations do not fit as easily with the most commonly mentioned normal modes. However, the periods of the different normal modes vary with the conditions, which is why they are usually named as "quasi-periods". As an example the (1,2) first antisymmetric mode has been measured with periods between 8 and 14 days (Hiroata and Hirooka 1984).

Indeed, according (Salby 1981) most of the variance for the (1,2) mode should lie in the interval $T \in (8.3, 10.6)$ days, making the 8.5-day wave another possible candidate for the quasi 10-day wave. In the same paper, Salby also found that the variance for the quasi 16-day period should usually be confined to the interval $T \in (11.1 - 20.0)$ days, making both the 11-13 day oscillation and the 14-15 day oscillation other possible candidates for the quasi 16-day wave.

As previously mentioned, the Lomb normalized periodogram does not give any information about the time at which a given frequency was found. It might be that the several different waves found that could correspond to a given normal mode did not appear at the same time, but rather as one normal mode whose period is shifted throughout the year. If it was possible to decide the time of strongest observations for each of the waves found in the datasets, it might be possible to determine if this is the case or whether the waves occurred at the same time.

From the 14-15 day and 17-20 day variations it can be seen that the 14-15 day wave roughly maximizes before and after midwinter, while the 17-20day wave has its maximum during midwinter. Therefore, these two might be one normal mode whose frequency changes, but without information about how their frequencies changes with time it cannot be said for sure.

No suitable corresponding normal modes can be found for the 26-45 day interval, despite its lack of increasing amplitude with altitude making it unlikely to be a propagating wave. This might further support the theory that the 26-45 day interval does not contain a single wave after all, but rather a superposition of shorter wave motions.

None of the waves found in this thesis appear to have amplitudes that increase with altitude, as is expected from propagating waves due to energy conservation and exponentially decreasing air density. It therefore seems likely that most or all of them are normal modes, not propagating but traveling westward with the atmosphere.

The direction the waves travel or propagate in cannot be recovered from the data used in this thesis, as all measurements are confined to two fixed locations, above the two research stations. To confirm or refute that the oscillations found in the ozone and temperature data are westward-traveling normal modes, analysis data should be used to find their direction of travel/propagation. By observing the wave amplitudes at several different locations at given times and altitudes the currently missing information about travel/propagation directions can be found.

In short, the observed oscillations lack the amplification with altitude usual for propagating waves and therefore appear likely to be westward traveling normal modes, though analysis data is necessary to confirm or deny the traveling direction. Most of the wave-periods fit with known periods of the normal modes, sometimes with more than one oscillation fitting with a given normal mode. This might be due to the periods of the normal modes changing throughout the year. However, since the information given about the wave frequencies does not include the time of a given oscillation this cannot be confirmed, though the variations throughout the year appear to support the theory, at least for the 14-15 and 17-20 day waves.

5.4 Ozone maxima

In all the isolated and filtered wave motions, one or more maxima in the variations can be seen. The model of percentage ozone variations due to a change in temperature presented in section 2.4 indicate that the amplitude of the percentage variations should be approximately constant with altitude. Because of this, increases in the variation amplitudes with altitude can be indicative of higher ozone mixing ratios. By looking for areas of stronger variations in the results it should be possible to identify ozone mixing ratio maxima both in the total non-seasonal variations and in the individual isolated and filtered wave motions.

The first and most obvious is found at the lowest altitudes included in the analysis. For most of the isolated oscillations the largest percentage variations in ozone can be

found at the interval ranging from 35 to 45km. This is clearly due to the first ozone maximum, which can be found at altitudes close to 35km for the ozone mixing ratios.

The secondary ozone maximum lies too high to be visible in the ozone data used here, but the tertiary maximum at altitudes close to 72km can be observed at the highest altitudes of the ozone data used in the analysis. The tertiary ozone maximum is a night-time phenomenon, but since only ozone mixing ratios measured at a time when the solar elevation was lower than $-10°$ have been used, it should be visible in the results.

Local maximum values can indeed be found at altitudes between 70 and 75km for most of the filtered oscillations. They are somewhat smaller than the ones found in the 35-45km altitude interval, but they are still clearly visible in most of the results. One exception is the 21-24 day oscillation where the ozone mixing ratios appear to be of approximately the same value all the way from approximately 65km up to 75km.

For some of the oscillations, the values at 87km are larger than those in the 70-75km interval. This is most notable for the 4-day and 11-13 day motions, but is also the case for the 5, 8-9 and 26-45 day intervals. However, the values at this altitude are based on temperature data, and do not reflect the ozone mixing ratios. When looking only at the region below 75km, maximum values do indeed appear at 35-45 km and 70-75km, where the first and tertiary ozone maxima can be found.

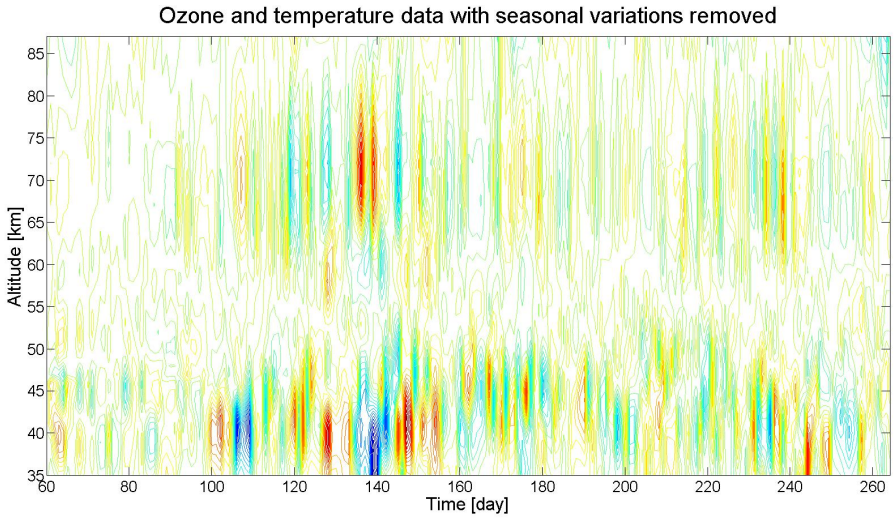

Figure 12: Percentage variations of ozone and temperature, with seasonal variations filtered out. Ozone up to 75km, temperature at 87km. The values for temperature have been multiplied by -6 to make them appear on the same scale as the ozone variations.

Looking at the overall picture of ozone and temperature variations with nothing but seasonal variations filtered out, Figure 12, also shows maximum ozone mixing ratios in the intervals 35-45km and 70-75km. So the first and tertiary ozone maxima can be observed both in the total non-seasonal variations and in each of the filtered frequency intervals.

5.4.1 Annual variations in the tertiary ozone maximum

In section 2.4.2 the annual variations of the tertiary ozone maximum were described. Measurements have shown it to have an annual maximum some time before the winter solstice, followed by a relative minimum in the following months. A second, somewhat smaller maximum then appears around the spring equinox, before the absolute minimum during summer.

After having removed all measurements of too high solar elevation, the datasets used in this thesis only cover the time period from the beginning of March to the middle of October 2009, so the summer values are not included. However, both the midwinter and spring equinox should be there.

For the oscillations with short periods, up to 10-11 days, the values at the altitudes of the tertiary ozone maximum do not vary significantly with time, apart from a gradual decrease towards the end of the datasets, and some variations for the 4-day wave. Neither can the expected changes of the tertiary maximum be seen in the 11-13 day oscillation.

Though several of the oscillations reach a maximum just before midwinter, and then decline, only the 14-15 and 26-45 day wave motions display both the pre-winter maximum and the next maximum close to the spring equinox. Variations in the 14-15 day oscillation can be seen in Figure 13.

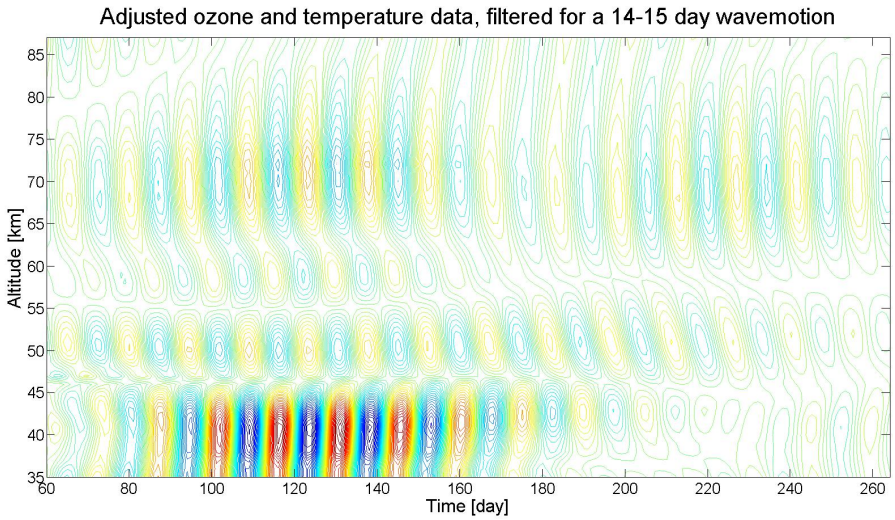

Figure 13: Percentage variations in ozone and temperature for the 14-15 day oscillation. Variations similar to those expected from the tertiary ozone maximum can be seen at altitudes close to 72km.

For the 14-15 day oscillation both maxima can be clearly seen, but they appear somewhat earlier in the year than what would be expected from the theory on the tertiary maximum. And for the 26-45 day interval, the break down of the few consistent wave structures during the Antarctic spring makes it hard to be sure if the apparent maxima

close to the spring equinox really is a maximum or wave motions reappearing after having vanished during the early spring.

In the total non-seasonal variations found in Figure 12, the ozone mixing ratios at the altitudes of the tertiary ozone maximum seem to reach a maximum value in late May (day 140), diminish, and then reach another smaller maximum value in the middle of August (day 240), the same as for the 14-15 day oscillation. The lowest values are found in the early Antarctic autumn, as expected since the absolute minimum appears during the summer.

In short, some variations similar to the expected annual variations of the tertiary ozone maximum were found in the altitude interval 70-75km for the overall non-seasonal variations, as well as some of the isolated frequency intervals. However, this was not the case for most of the oscillations, and even for the oscillations where they did appear both of the maxima appeared somewhat earlier than expected. This might be at least partially due to other effects. For example some of the waves might have a vertical wavelength in addition to the horizontal, or their frequencies might have shifted with time, making the amplitudes of the oscillations appear weaker than they are. A test of such filter effects is made in section 5.6.

5.5 Wind fields

In the troposphere, the mean zonal winds are generally westward at low latitudes and eastward with two clear jet streams at mid-latitudes. At higher altitudes, in the stratosphere and mesosphere, the mean zonal winds are generally eastward during the winter and westward during the summer, changing direction near the mesopause in the time period around the equinoxes (Andrews 2000). During stratospheric warmings the wind direction also turns from eastward to westward. The maximum velocities can generally be found in the mid-latitude mesosphere during the summer and winter solstices, (Fleming et al. 1990).

Monthly mean winds above Rothera (68°S, 68°W) can be seen in Figure 14. Examples of mean zonal winds as functions of latitude and height for January and June can be seen in the appendix Plots, Figure 19 and 20.

Since all the measurements used in the analysis are from the Antarctic autumn, winter and spring, the wind field would be expected to be weak at first, then become dominated by eastward winds. As the wind fields weaken and change direction close to the equinoxes, it would be expected that any attenuation above the main wind field at 40-60km would be stronger during midwinter than during autumn and spring.

As seen in Chapter 2.1.6, planetary waves are only able to propagate vertically in winds that are eastward relative to the phase velocity of the wave, and that are below a critical limit U_c. The value of this critical limit depends on the wave, so different waves will have different critical levels of wind in which they are unable to propagate.

Planetary waves meeting westward winds will be absorbed and disappear. Meeting moderate eastward winds slower than the critical limit of the waves will result in a

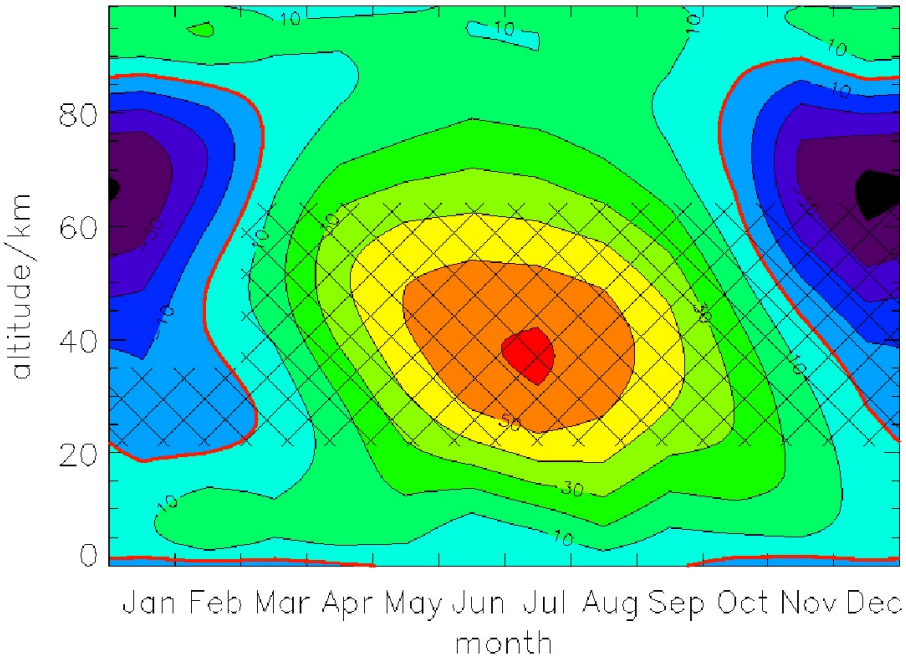

Figure 14: Mean zonal wind above Rothera from 0-100km. Generated from 6th order polynomial fits to the monthly mean data and, within the hatched area, monthly mean HWM-93 model winds. The thich red line represents the $0ms^{-1}$ contour, other contours are drawn at $10ms^{-1}$ intervals. Blue colour: westward winds. From (Hibbins et al. 2005)

moderate phase-shift of the waves in the region of the wind field, and a continued vertical propagation above the altitudes of the winds. If the planetary waves meet very strong eastward winds, the phase is strongly displaced and the waves become evanescent in this region. However, they can reappear above the strong wind field. An example of both of these situations can be seen in Figure 15, showing a detail from the 10-11 day oscillation. At 49km the phase is strongly shifted, and the waves can no longer be observed, while between 54 and 56km the phase of the wave appears to have been displaced by the eastward winds.

From Figure 14 it can be seen that the strongest part of the mean zonal wind field is found higher during the Antarctic summer than during the winter, which is in agreement with the general shape of the "empty bands" seen in the isolated wave motions. In the figure, the strongest winds can be found at altitudes close to 40km, while the bands seen in the isolated waves are strongest in the interval 40-60km, varying from wave to wave. It seems likely that the bands seen in the isolated waves are due to strong eastward winds temporarily attenuating or wiping out the waves. It should again be noted that apparently weak or empty bands between 75 and 87km are due to a lack of data and this region.

The differences in the exact altitude of the strongest bands found in the isolated waves might be due to a combination of different critical levels for the different waves, and

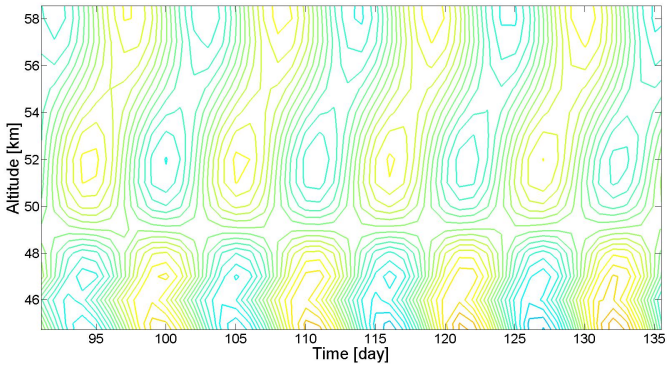

Figure 15: Detail of the 10-11 day oscillation, showing possible evanescence at 49km and phase displacement at 54-56km.

one or more of the isolated waves having a vertical wavelength in addition to their horizontal ones. Such vertical wavelengths might also be responsible for some of the differences between the waves in regard to the vertical and annual variations of the ozone maxima described in section 5.4.

Only the large planetary-scale waves are able to propagate vertically through the strong eastward winds found in the stratosphere during winter, smaller disturbances are trapped before they get far above the tropopause. And during summer westward winds in the stratosphere prevent all wave motions from propagating vertically (Salby 1996).

As all the wave motions found in the ozone data are able to pass through the wind field at 40-60km, they appear to be planetary waves that the eastward winter wind is not strong enough to completely stop from propagating up into the stratosphere and mesosphere. However, the wind does weaken some of the oscillations, especially the long period ones.

From the theory, it is known that planetary waves with short wavelengths often have a slow eastward group velocity, while planetary waves with medium wavelengths are stationary, and those with long wavelengths have a quick, westward group velocity. In addition, waves with long wavelengths can propagate vertically in a larger range of eastward flows than waves with shorter wavelengths. The shorter wavelength waves with small group velocities tolerate less strong westward winds, but stronger eastward winds than those with higher velocities.

The amplitudes of the shortest-period wave motions did not get attenuated by passing through the strongest wind field, while the longer period waves were attenuated. This further strengthens the theory of the isolated oscillations being the resonant normal modes of the atmosphere. According to (Salby 1981), influences that degrade the resonant response of normal modes, such as wind, increase with both wavenumber s and meridional index n. The 4- and 5-day waves were identified as likely to be the (2,1) and (1,1) normal modes, having very long wavelengths and being able to withstand stronger eastward winds than the higher modes.

5.6 Filter effects

In order to see how the chosen frequency limits for the filters used in isolating each wave motion influenced the result, the 14-15 day motion was filtered again, this time with a more narrow filter. The choice of the 14-15 day wave motion for this test was rather arbitrary, any of the oscillations consisting of a single motion would do, excluding only the 26-45 day possible superposition and the 11-13 day oscillation appearing to consist of two different frequencies at low altitudes. The more narrowly filtered 14-15 day wave can be found in Figure 39 in the appendix Plots.

A narrower filter would be expected to result in weaker variations in areas with strong winds, or other regions where the dominating frequency of the wave motion shifts.

The expected weakening in the wind fields is due to the wind shifting the phase/frequency of the oscillation. This effect would be increased by using more narrow filters. As the frequency of the oscillation is shifted, it might move towards the limits of the filter passband, or even pass outside the filter limits. This would further diminish the wave amplitude according to the attenuation set for the filter.

The same effect is expected in areas where the oscillation frequency changes for other reasons. Small frequency shifts would result in a weak attenuation of the oscillation amplitude, while larger shifts would lead to a stronger attenuation, until the oscillation eventually is completely removed by the filter.

For the 14-15 day wave the weak bands in the variations corresponding to the wind field did not significantly broaden with the more narrow filter compared to the original isolated 14-15 day wave. This indicates that while the effect of the wintertime eastward wind is strong enough to attenuate the oscillation in the region of the strongest wind field, it does not displace the frequency of the oscillation enough to bring it outside of the filter limits for any of the two filters.

However, the narrow filter did result in an overall weakening of the oscillation with time. From day 200 and onward the oscillations were clearly weakened compared to the results from the original filter.

This can be explained by an observation made in section 5.2; that the period of the 14-15 day wave appears to increase with time, gradually moving from closer to 14 days to closer to 15 days. As the frequency became lower, it moved towards the limits of the new, narrow filter and was attenuated, resulting in an apparent weakening of the oscillation with time.

The important point to note from this section is that due to filter effects a displacement of frequency towards the filter limits might result in an apparent weakening of the oscillation. Changes in the strength of the variations might therefore be a result of different ozone mixing ratios at different altitudes, vertical wavelengths of the waves, or winds or other effects leading to changes in the frequency dominating the oscillation, and not necessarily a weakening or strengthening of the wave itself with altitude.

6 Conclusion and future work

Ozone data from the ARON millimeter wave spectrometer at Troll Station (72°S, 2°E) and temperature data from the OH Meinel (3,1) band in the hydroxyl airglow measured by the Michelson interferometer at Rothera ($68°S$, 68°W) has been analyzed, covering the period from the beginning of March to the middle of October 2009. Consistent wave structures were found in both datasets, all the way from 35km to 87km with only temporary gaps in the areas of strong wind fields.

The waves were found in frequency bands corresponding to 4, 5, 8.5, 10-11, 11-13, 14-15, 17-20, 21-24 and 26-45 day bands, with the 26-45 day variations likely being due to a superposition of smaller waves. The 4- and 5-day oscillations fit with the (2,1) and (1,1) normal modes frequently observed in the atmosphere, and several of the others seem to fit to other normal modes, sometimes more than one to a given mode.

This might be due to the frequency changing throughout the year, as the Lomb normalized periodogram does not give any information about the time at which a given frequency dominated the spectrum. It therefore can not be said for sure whether several of the observed oscillations belong to a single normal mode whose frequency changes throughout the year. The variations seen in for example the 14-15 and 17-20-day waves maximize at different times of the year, indicating that they might both be the quasi 16-day normal mode, with a time-varying frequency. Looking further into the development of the frequencies throughout the year could confirm or refute whether this is the case.

Other future work could include finding the directions in which the different waves travel or propagate. For this, the millimeter wave spectroscopy-measurements do not give enough information, as they are all measured above a specific location. Analysis data, for example from the ECMWF might be used to observe the waves at several different latitudes at the same time, giving enough information to determine the travel/propagation direction.

The observed waves have several of the characteristics of planetary waves and the atmospheric normal modes. In addition to the observed periods fitting with those of the most commonly observed normal modes, the wave amplitudes do not increase with altitude. This is as expected for the normal modes, and unlike propagating planetary waves whose amplitudes increase with decreasing atmospheric density.

The ozone mixing ratio percentage variations do change with altitude, but this is most likely to be due to the ozone mixing ratio changing with altitude, and perhaps also to shifts in the frequency, or the waves having vertical wavelengths as well as horizontal. Both the first and tertiary ozone maximum can be observed in the ozone variations, and variations throughout the year consistent with those expected from the tertiary ozone maximum can be seen in some of the isolated oscillations.

The waves are able to propagate vertically through the strong eastward wind fields found at altitudes around 40-60km during the Antarctic winter, a trait typical for the large horizontal-scale planetary waves. Smaller waves are trapped near the surface and

should not be found above the wind fields. The attenuation, or lack of attenuation of the different waves does fit with the theory of the 4- and 5-day waves being the (2,1) and (1,1) normal modes, with the longer period waves belonging to higher modes. The longer-period waves are seen to be attenuated when passing through the wind field, which is in accordance with the theoretical higher modes being more vulnerable to zonal winds.

Temperature data from hydroxyl airglow has successfully been used to trace planetary waves in the past, providing a practical yardstick to compare the results from the ozone up against. Finding the same wave motions in ozone data as in the temperatures indicate that millimeter wave spectrometry is a viable technique for tracing planetary waves in ozone in a part of the atmosphere that is otherwise expensive or time consuming to measure.

References

[Allen et al. 1984] Allen, M., Lunine, J.I., Yung, Y.L., *The Vertical Distribution of Ozone in the Mesosphere and Lower Thermosphere* Journal of Geophysical Research, Volume 89 (D3), Pages 4841-4872, 1984

[Andrews 2000] Andrews, D.G., *An Introduction to Atmospheric Physics*, Cambridge University Press, 2000

[Andrews et al. 1987] Andrews, D. G., Holton, J.R., Leovy, C.B., *Middle Atmosphere Dynamics*, International Geophysics Series, Volume 40, Academic Press, 1987

[Brasseur and Solomon 2005] Brasseur, G., Solomon, S., *Aeronomy of the Middle Atmosphere - Chemistry and Physics of the Stratosphere and Mesosphere*, 3rd edition, Springer, 2005

[Espy et al. 2006] Espy, P.J., Hartogh, P.,Holmn, K., *A microwave radiometer for the remote sensing of nitric oxide and ozone in the middle atmosphere*, Proceedings of SPIE, Vol 6362, 63620P, 2006

[Espy 2010] Espy, P.J., *Lecture 2 - Overview of the Atmosphere*, Lecture notes FY3201, Atmospheric Physics, 2010

[Fleming et al. 1990] Fleming, E.L., Chandra, S., Barnett, J.J., Corney, M., *Zonal mean temperature, pressure, zonal wind and geopotential height as functions of latitude*, Advances in Space Research, Volume 10, No. 12, Pages (12)11-(12)59, 1990

[Forbes 1995] Forbes, J., *Tidal and Planetary waves*, *The upper mesosphere and lower thermosphere: a review of experiment and theory (Geophysical Monograph)*, Johnson, R.M., Killeen, T.L, Pages 67-87, 1995

[Hartogh at al. 2004] Hartogh, P.,Jarchow, C., Sonnemann, G.R., Grygalashvyly, M., *On the spatiotemporal behaviour of ozone within the upper mesosphere/mesopause region under nearly polar night conditions* Journal of Geophyscal Research, Volume 109, D18303, doi:10.1029/2004JD004576, 2004

[Hertzberg 1950] Herzberg,G., *Molecular Spectra and Molecular Structure, I. Spectra of Diatomic Molecules*, Chapter 3, D. Van Nostrand Company Inc., 1950

[Hibbins et al. 2005] Hibbins, R.E., Shanklin, J.D., Espy, P.J., Jarvis, M.J., Riggin, D.M., Fritts, D.C., Lübken, F.J., *Seasonal variations in the horizontal wind structure from 0-100km above Rothera station, Antarctica (67° S, 68° W)*, Atmospheric Chemistry and Physics, 5, Pages 2973-2980, 2005

[Hiroata and Hirooka 1984] Hirota, I., Hirooka, T., *Normal Mode Rossby Waves Observed in the Upper Stratosphere. Part I: First Symmetric Modes of Zonal Wavenumbers 1 and 2*, Journal of the Atmospheric Sciences, Volume 41, No. 8, Pages 1253-1267, 1984

[Houghton 2002] Houghton, J., *The Physics of Atmospheres*, Third edition, Cambridge University Press, 2002

[Kleinknecht 2010] Kleinknecht, N., *Planetary Wave Oscillations Observed in Ozone from Troll Station Antarctica* Master Thesis, NTNU, 2010

[Koblick 2009] Koblick,D., http://www.mathworks.com/matlabcentral/fileexchange/23051-solar-azimuth-and-elevation-estimation, 2009

[Kormylo and Jain 1974] Kormylo, J.J., Jain, V.K., *Two-Pass Recursive Digital Filter with Zero Phase Shift* IEEE Transactions on Acoustics, Speech and Signal Processing, Volume 22, Issue 5, Pages 384-387 1974

[Krüger et al. 2005] Krüger, K., Naujokat, B., Labitzke, K., *The unusual midwinter warming in the Southern Hemisphere stratosphere 2002: a comparison to Northern Hemisphere phenomena*, Journal of the Atmospheric Sciences, Volume 62, Pages 603-613, 2005

[Kuntz et al. 1997] Kuntz, M., Hochschild, G., Krupa, R., *Retrieval of ozone mixing ratio profiles from ground-based millimeter wave measurements disturbed by standing waves*, Journal of Geophysical Research, Volume 102, No. D18, Pages 21.965-21.975, 1997

[Lund 2010] Lund, H., *Variation of the hydroxyl near infrared airglow at Rothera, Antarctica (68°S, 68°W)* Master Thesis, NTNU, 2010

[Lynch and Cassano 2006] Lynch, A.H., Cassano, J.J., *Applied Atmospheric Dynamics*, Chapter 8, John Wiley & Sons, 2006

[Marsh et al. 2001] Marsh, D., Smith, A., Kaufmann, M., Grossmann, K., *The existence of a tertiary ozone maximum in the high-latitude middle mesosphere*, Geophysical research letters, Volume 28, No. 24, Pages 4531-4534, 2001

[NPI 2006] Norsk Polarinstitutt, "Troll i ord - ord om Troll", http://npweb.npolar.no/Artikler/2006/1158735080.33, 2006

[Pendleton et al. 1993] Pendleton, W.R., Espy, P.J., Hammond, M.R., *Evidence for Non-Local-Thermodynamic-Equilibrium Rotation in the OH Nightglow*, Journal of Geophysical Research, Volume 98, Pages 11567-11579, 1993

[Press and Rybicki 1988] Press, W.H., Rybicki, G.B., *Fast algorithm for spectral analysis of unevenly sampled data*, The Astrophysical Journal, 338:227-280, 1988

[Press et al. 1992] Press, W.H., Plannery, B.P., Teukolsky, S.A., Vetterling, W.T., *Recipes in Fortran 77: The Art of Scientific Computing*, Chapter 13.8, Cambridge University Press, 1992

[Randel 1992] Randel, W.J., *Global Normal-mode Rossby Waves Observed in Stratospheric Ozone Data*, Journal of the Atmospheric Sciences, Volume 50, No. 3, Pages 406-420, 1992

[Rodgers 1976] Rodgers, C.D., *Retrieval of Atmospheric Temperature and Composition From Remote Measurements of Thermal Radiation*, Reviews of Geophysics and Space Physics, Volume 14, No. 4, 1976

[Salby 1981] Salby, M.L., *Rossby Normal Modes in Nonuniform Background Configurations. Part II: Equinox and Solstice conditions*, Journal of the Atmospheric Sciences, Volume 38, No. 9, Pages 1827-1840, 1981.

[Salby 1984] Salby, M.L., *Survey of Planetary-Scale Travelling Waves: The State of Theory and Observations*, Reviews of Geophysics and Space Physics, Volume 22, No. 2, Pages 209-236, 1984

[Salby 1996] Salby, M.L., *Fundamentals of Atmospheric physics*, International Geophysics Series, Volume 61, Academic Press, 1996

[Sander et al. 2003] Sander, S.P., et al., *Chemical Kinetics and Photochemical Data for Use in Atmospheric Studies*, Evaluation Number 14, JPL Publication 02-25, 2003

[Saragiotis 2008] Saragiotis, C., http://www.mathworks.com/matlabcentral/fileexchange/22215-lomb-normalized-periodogram, 2008

[Sivjee 1992] Sivjee, G.G., *Airglow hydroxyl emissions*, Planetary and Space Science, Volume 40, Issues 2-3, Pages 235-242, 1992

[Smith and Marsh 2005] Smith, A.K., Marsh, D.R., *processes that account for the ozone maximum at the mesopause*, Journal of Geophysical Research, Volume 110, D23305, doi:10.1029/2005JD006298, 2005

[Sofieva et al. 2009] Sofieva, V.F, et al., *Spatio-temporal observations of the tertiary ozone maximum*, Atmospheric Chemistry and Physics, 9, Pages 4439-4445, 2009

[Sonnemann et al. 2006] Sonnemann, G.R., Grygalashvyly, M., Hartogh, P., Jarchow, C., *Behaviour of mesospheric ozone under nearly polar night conditions* Advances in Space Research 38, Pages 2402-2407, 2006

[Sonnemann et al. 2007] Sonnemann, G.R., Hartogh, P., Jarchow, C., Grygalashvyly, M., Berger, U., *On the winter anomaly of the night-to-day ratio of ozone in the middle to upper mesosphere in the middle to high latitudes*, Advances in Space Research 40, Pages 846-854, 2007

A Plots

A.1 Analysis

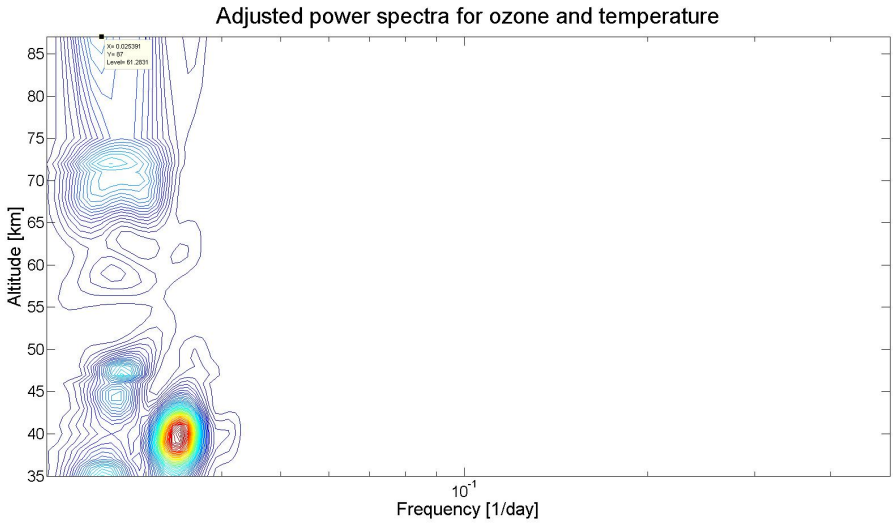

Figure 16: Power spectra for ozone and temperature, filtered for 26-45 day wavemotions. The x-axis has been plotted on a logarithmic scale to make it easier to see the variations in the dominating frequencies.

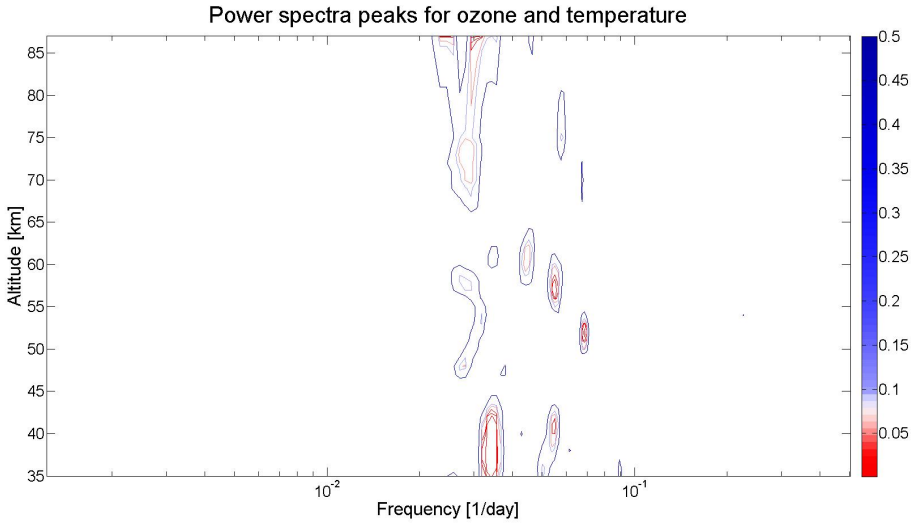

Figure 17: Lomb normalized periodograms, with the significance levels decided by the highest peak. The scale indicates the probability of a given peak being caused by noise

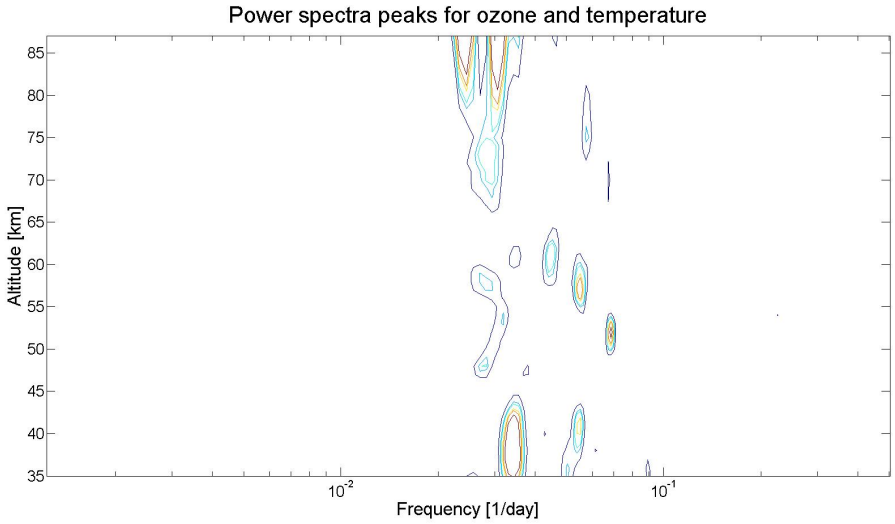

Figure 18: Lomb normalized periodograms, with significance levels decided by the second highest peak. The contour lines indicate 50%, 10%, 5%, 1% and 0.5% chance of being caused by noise.

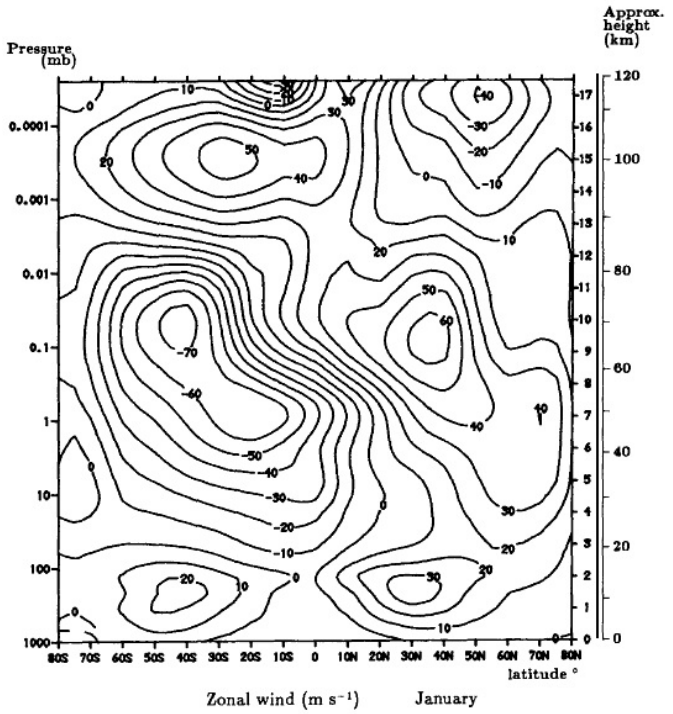

Figure 19: Zonal mean wind (ms^{-1}) for January, from the CIRA dataset. Negative values: westward winds. Positive values: eastward winds. From (Fleming et al. 1990)

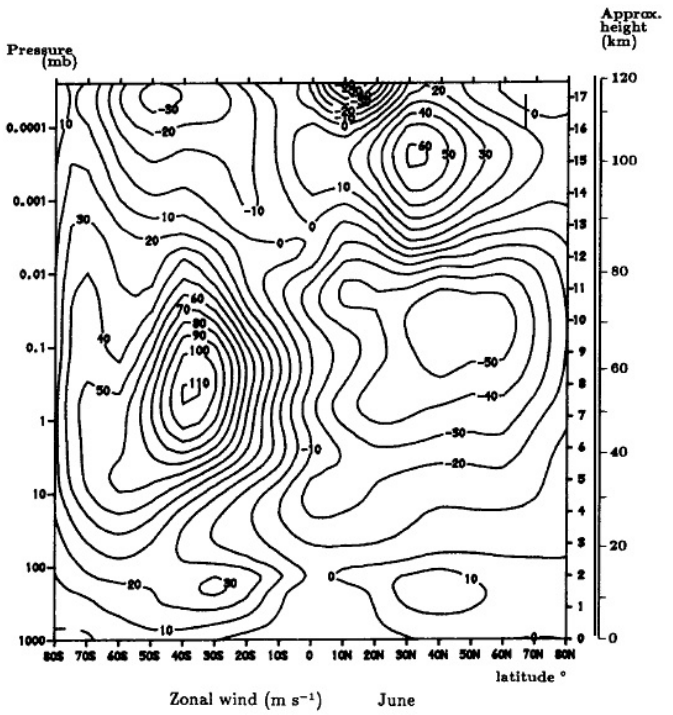

Figure 20: Zonal mean wind (ms^{-1}) for June, from the CIRA dataset. Negative values: westward winds. Positive values: eastward winds. From (Fleming et al. 1990)

A.2 Results

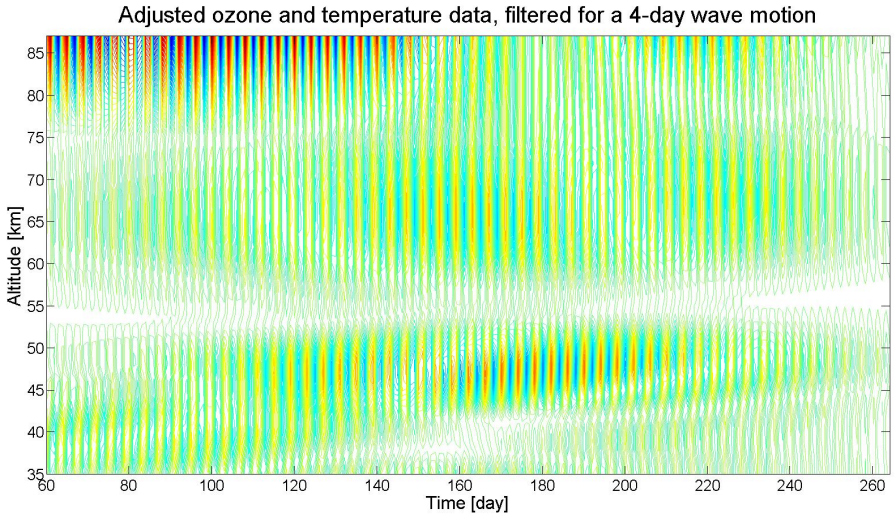

Figure 21: Percentage variations in ozone and temperature, filtered to allow only the 4-day wave motions to remain. The temperature data at 87km has been multiplied by -6 to make the waves more visible.

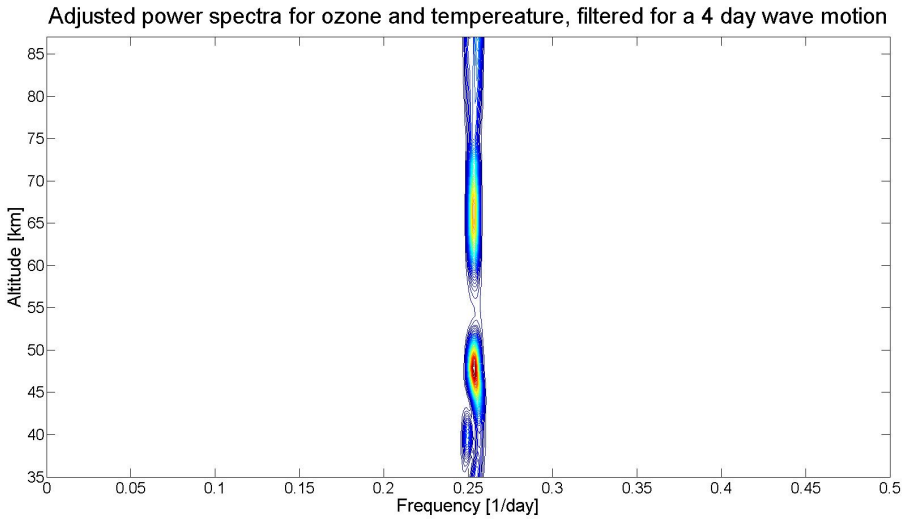

Figure 22: Power spectra for a 4-day wave motion. In order to make both datasets visible, values from 35-75km have been divided by the mean of all values for ozone, and values at 87km by the mean of all values for temperature.

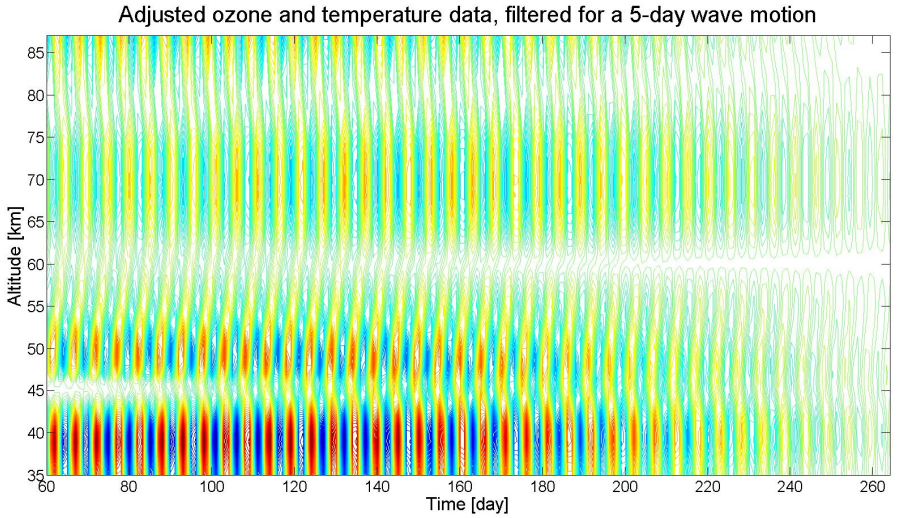

Figure 23: Percentage variations in ozone and temperature, filtered to allow only the 5-day wave motion to remain. The temperature data at 87km has been multiplied by -6 to make the waves more visible.

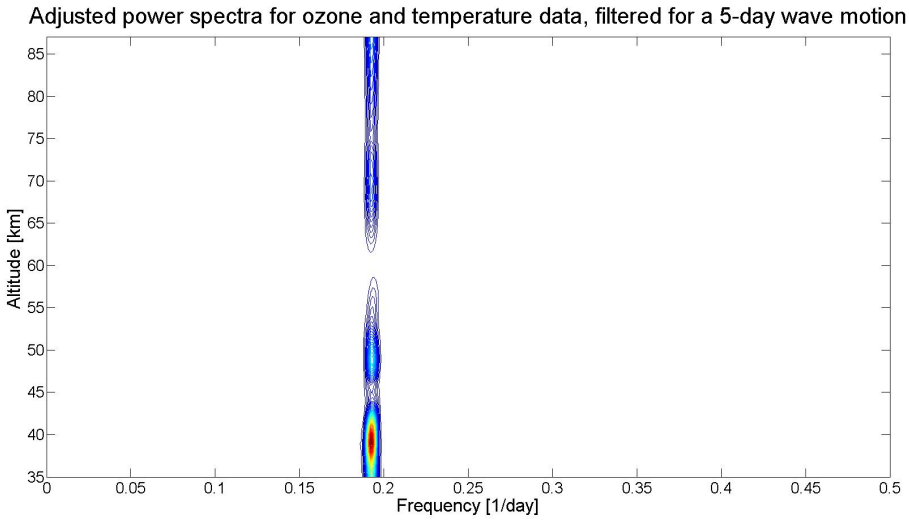

Figure 24: Power spectra for a 5-day wave motion. In order to make both datasets visible, values from 35-75km have been divided by the mean of all values for ozone, and values at 87km by the mean of all values for temperature.

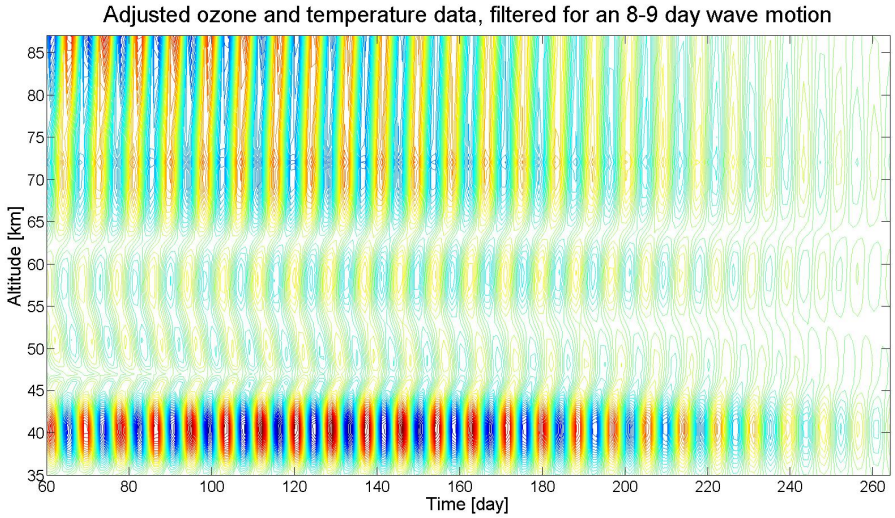

Figure 25: Percentage variations in ozone and temperature, filtered to allow only 8-9 day wave motions to remain. The temperature data at 87km has been multiplied by -6 to make the waves more visible.

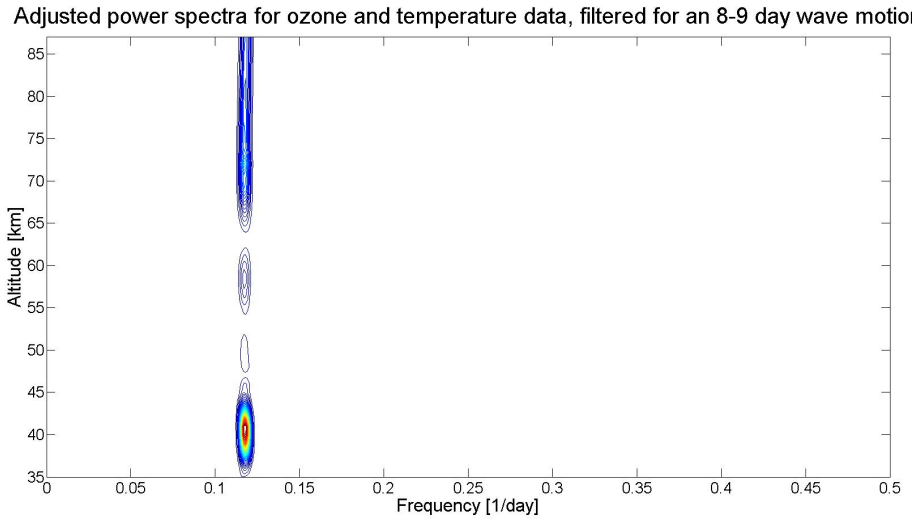

Figure 26: Power spectra for 8-9 day wave motions. In order to make both datasets visible, values from 35-75km have been divided by the mean of all values for ozone, and values at 87km by the mean of all values for temperature.

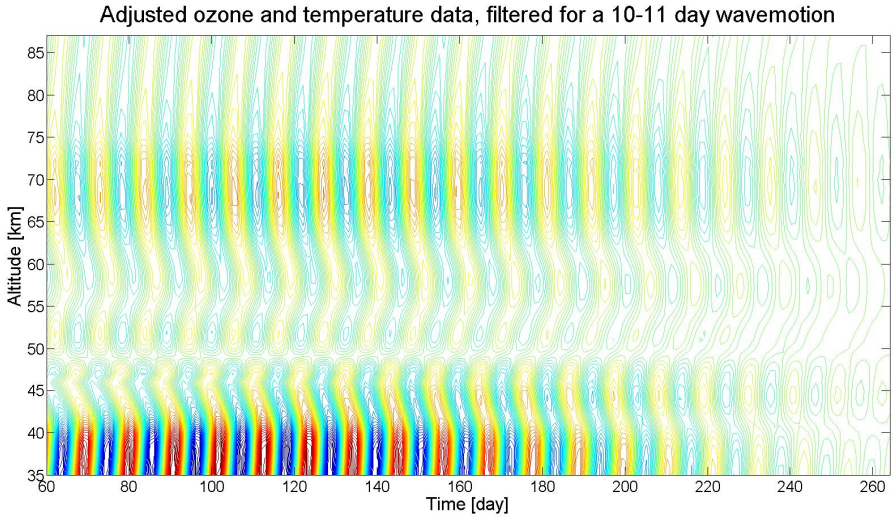

Figure 27: Percentage variations in ozone and temperature, filtered to allow only 10-11 day wave motions to remain. The temperature data at 87km has been multiplied by -6 to make the waves more visible.

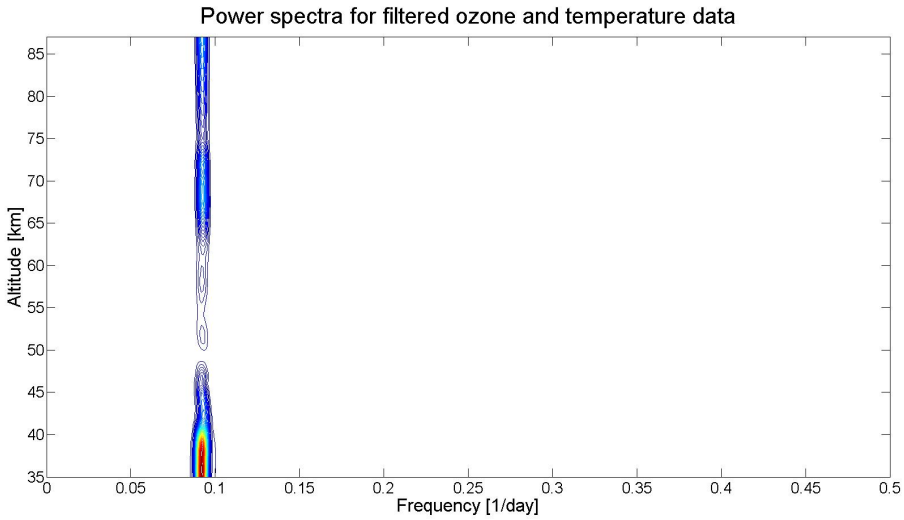

Figure 28: Power spectra for 10-11 day wave motions. In order to make both datasets visible, values from 35-75km have been divided by the mean of all values for ozone, and values at 87km by the mean of all values for temperature.

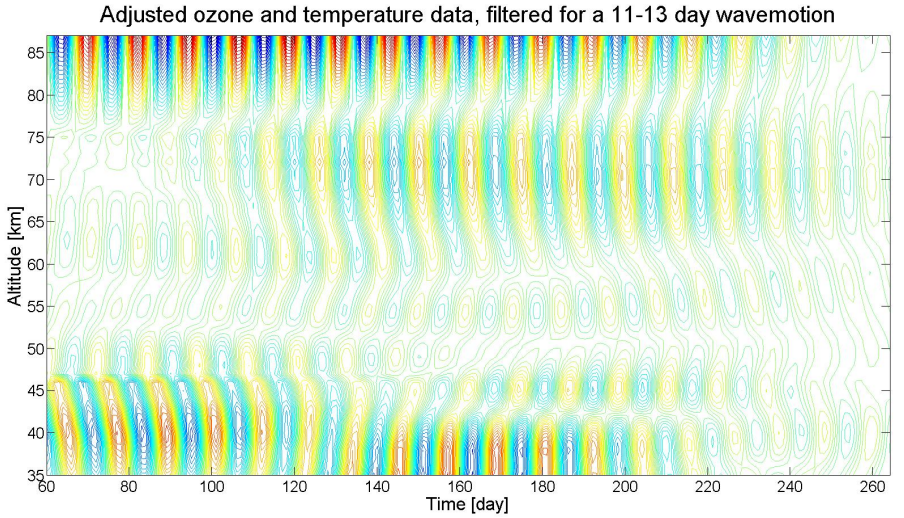

Figure 29: Percentage variations in ozone and temperature, filtered to allow only 11-13 day wave motions to remain. The temperature data at 87km has been multiplied by -6 to make the waves more visible.

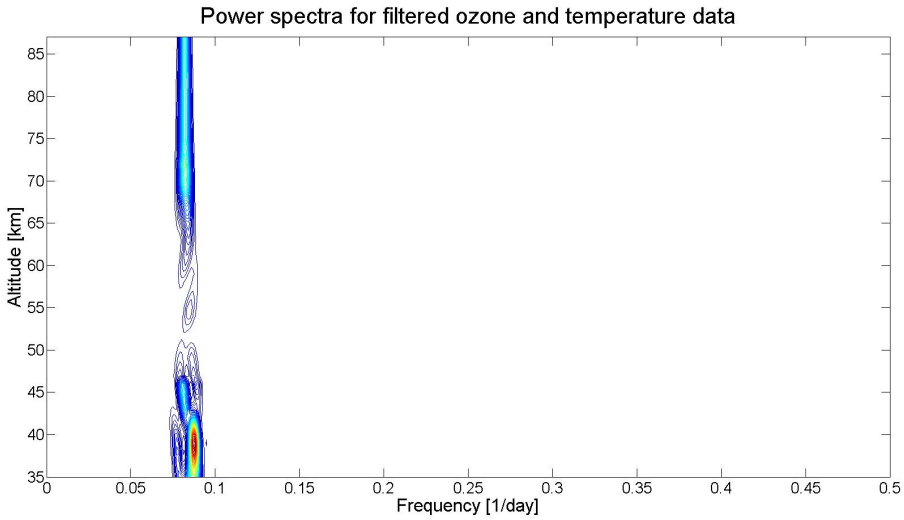

Figure 30: Power spectra for 11-13 day wave motions. In order to make both datasets visible, values from 35-75km have been divided by the mean of all values for ozone, and values at 87km by the mean of all values for temperature.

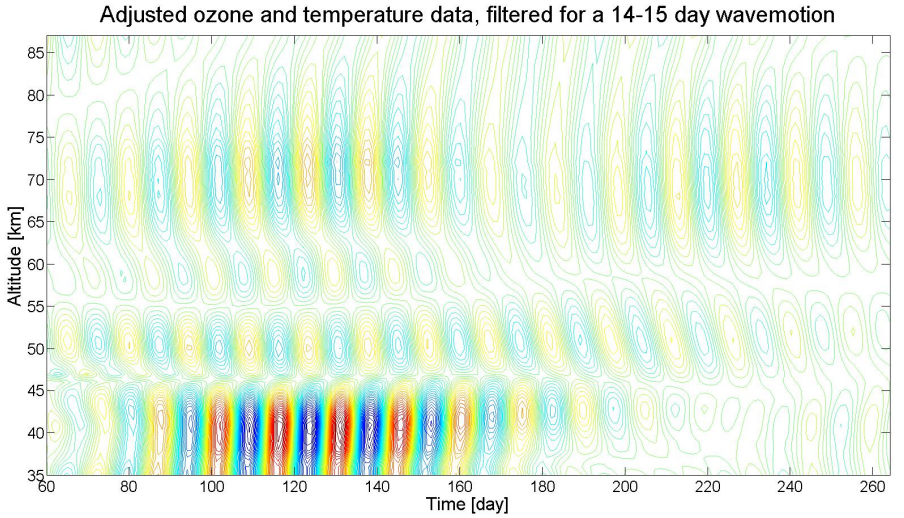

Figure 31: Percentage variations in ozone and temperature, filtered to allow only 14-15 day wave motions to remain. The temperature data at 87km has been multiplied by -6 to make the waves more visible.

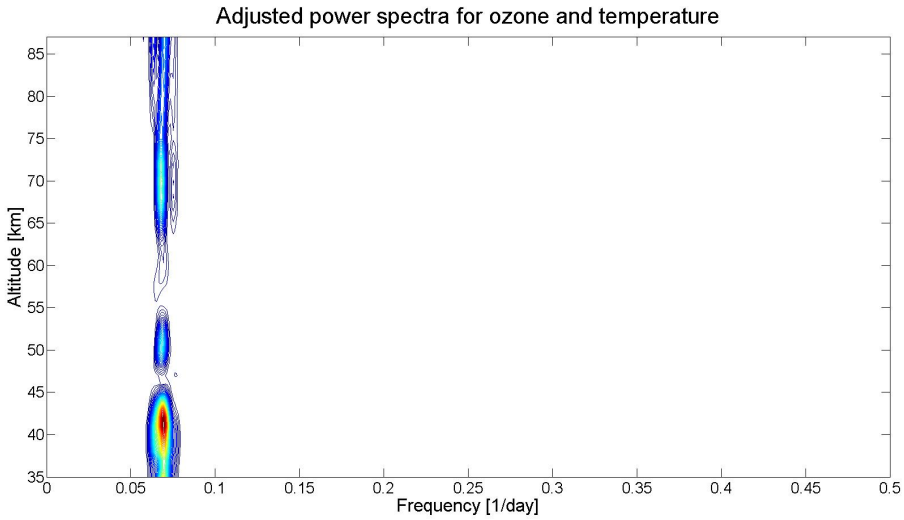

Figure 32: Power spectra for 14-15 day wave motions. In order to make both datasets visible, values from 35-75km have been divided by the mean of all values for ozone, and values at 87km by the mean of all values for temperature.

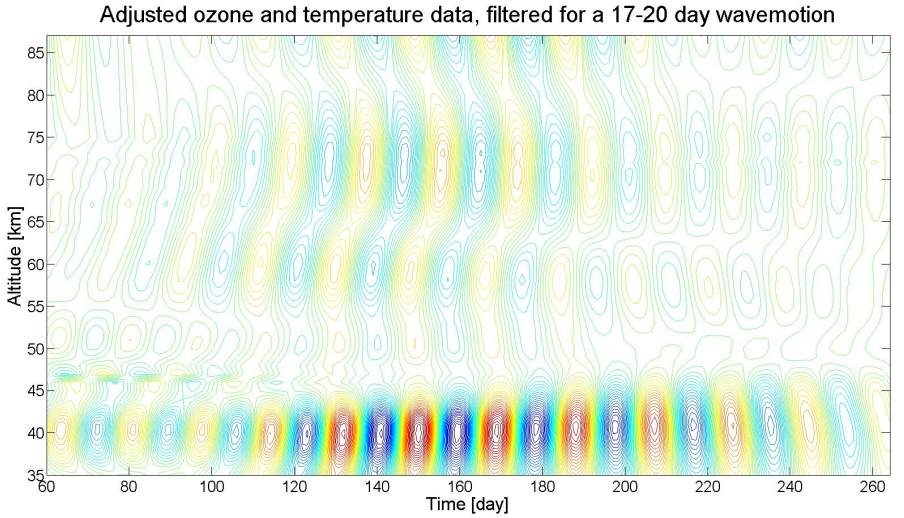

Figure 33: Percentage variations in ozone and temperature, filtered to allow only 17-20 day wave motions to remain. The temperature data at 87km has been multiplied by -6 to make the waves more visible.

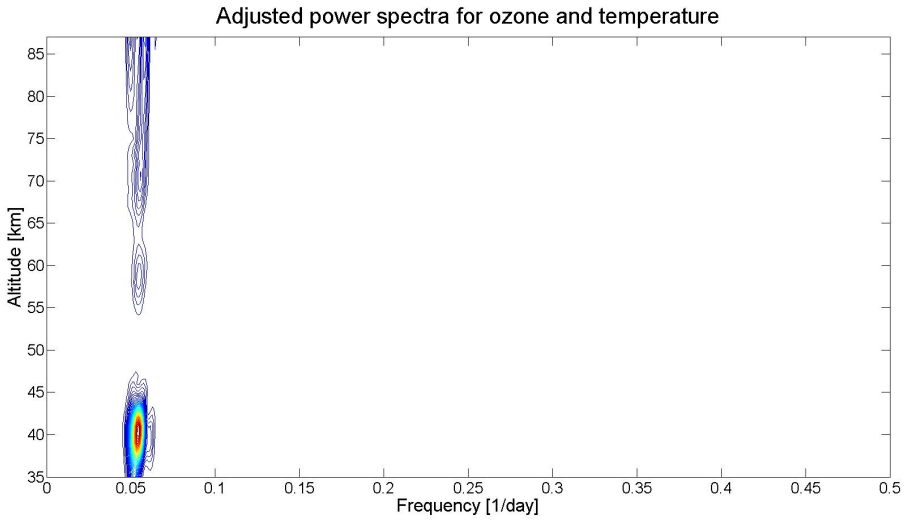

Figure 34: Power spectra for 17-20 day wave motions. In order to make both datasets visible, values from 35-75km have been divided by the mean of all values for ozone, and values at 87km by the mean of all values for temperature.

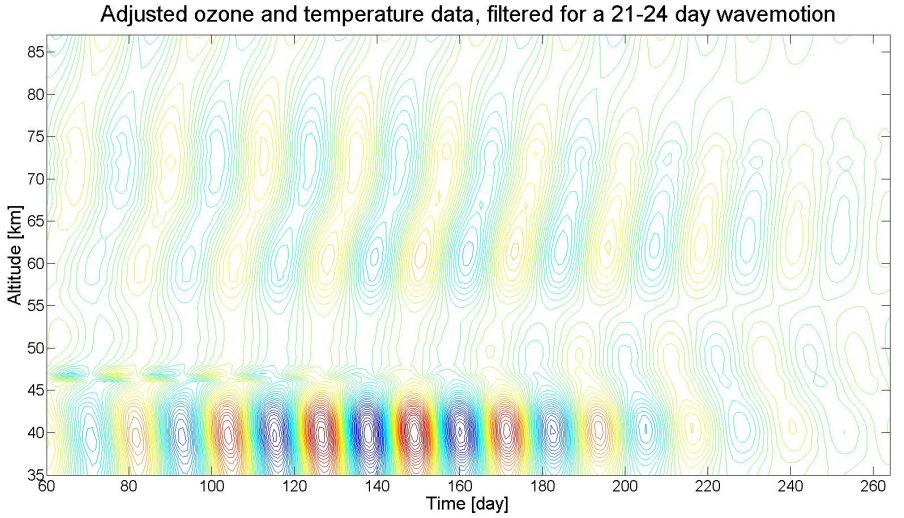

Figure 35: Percentage variations in ozone and temperature, filtered to allow only 21-24 day wave motions to remain. The temperature data at 87km has been multiplied by -6 to make the waves more visible.

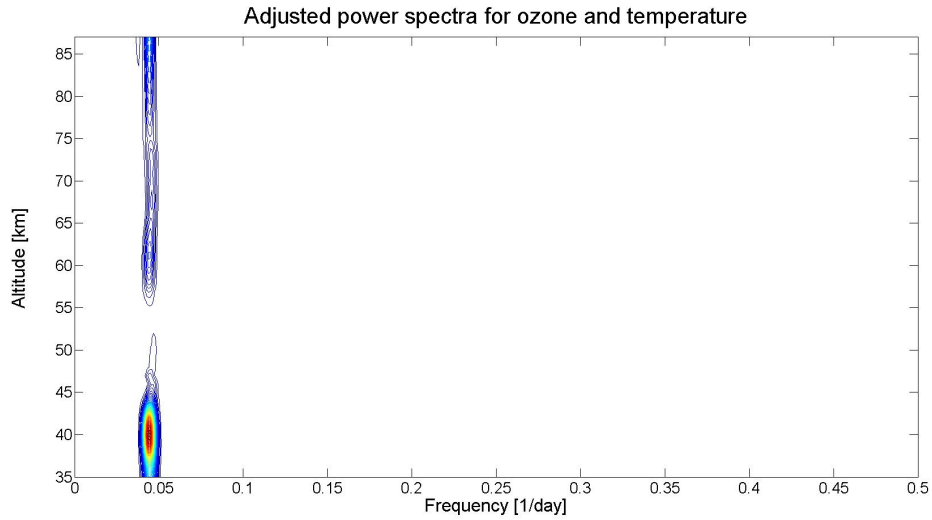

Figure 36: Power spectra for 21-24 day wave motions. In order to make both datasets visible, values from 35-75km have been divided by the mean of all values for ozone, and values at 87km by the mean of all values for temperature.

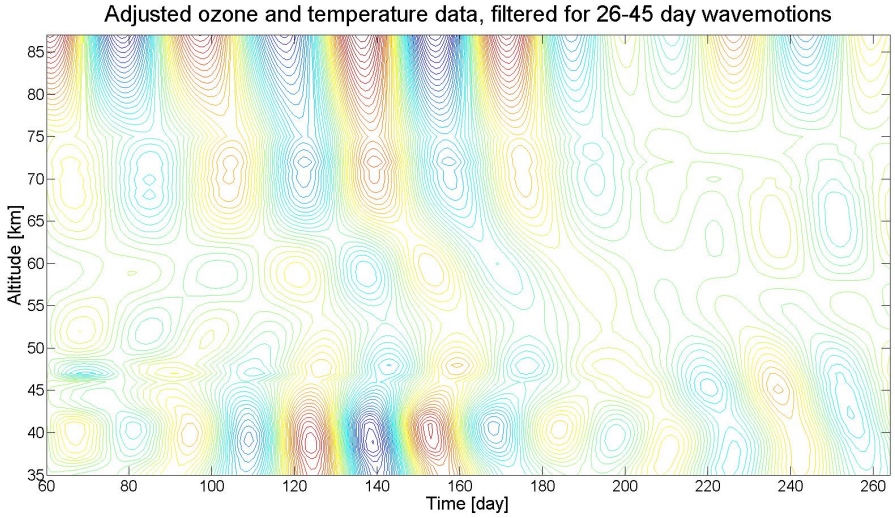

Figure 37: Percentage variations in ozone and temperature, filtered to allow only 26-45 day wave motions to remain. The temperature data at 87km has been multiplied by -6 to make the waves more visible.

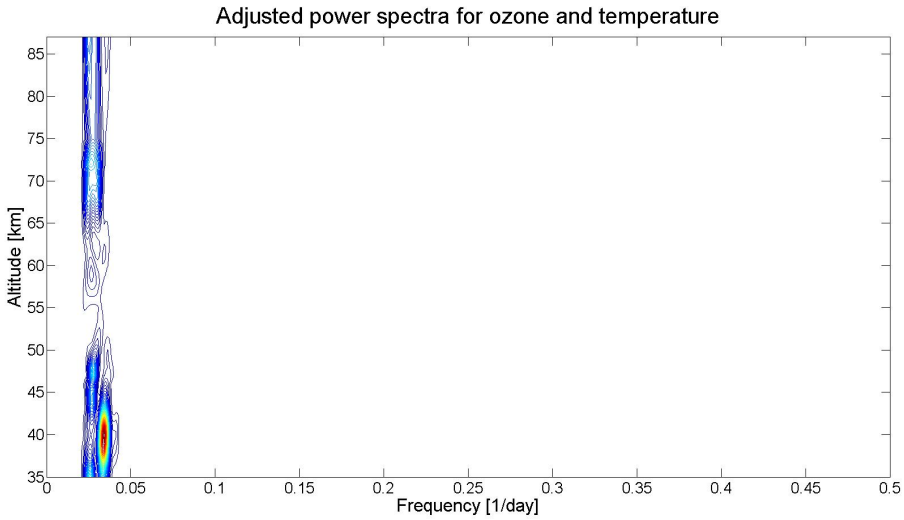

Figure 38: Power spectra for 26-45 day wave motions. In order to make both datasets visible, values from 35-75km have been divided by the mean of all values for ozone, and values at 87km by the mean of all values for temperature.

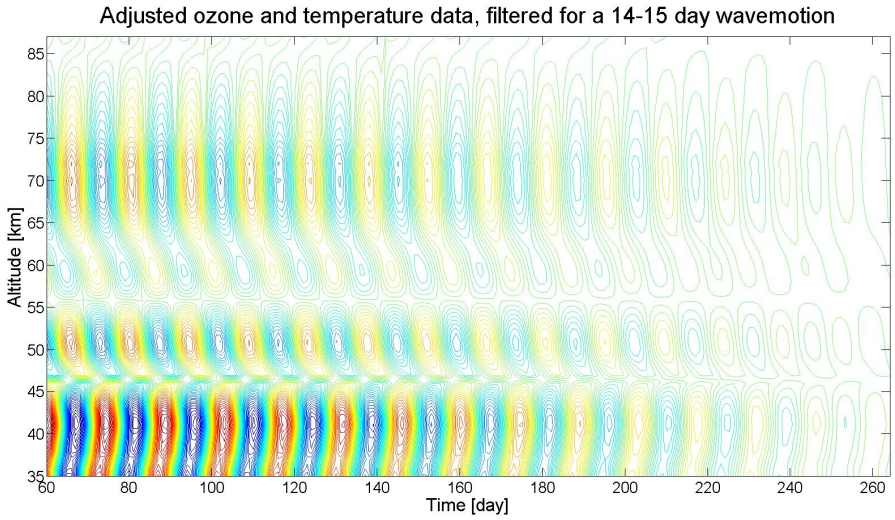

Figure 39: Narrow filter. The percentage variations in ozone and temperature for the 14-15 day wave, isolated with a more narrow filter in order to observe possible filter-effects.